Using Supercritical CO2 in the Preparation of Metal-Organic Frameworks: Investigating Effects on Crystallisation

Huan V. Doan [1,2], **Fei Cheng** [3], **Thandeka Dyirakumunda** [4], **Mark R. J. Elsegood** [4], **Jiamin Chin** [5], **Oliver Rowe** [6], **Carl Redshaw** [3,*] **and Valeska P. Ting** [1,*]

1   Department of Mechanical Engineering, University of Bristol, Bristol BS8 1TR, UK; huan.doan@bristol.ac.uk
2   Department of Oil Refining and Petrochemistry, Faculty of Oil and Gas, Hanoi University of Mining and Geology, Duc Thang, Bac Tu Liem, Hanoi 10000, Vietnam
3   Department of Chemistry & Biochemistry, University of Hull, Cottingham Rd, Hull HU6 7RX, UK; F.Cheng@hull.ac.uk
4   Chemistry Department, Loughborough University, Loughborough, Leicestershire LE11 3TU, UK; Thandeka.Dyirakumunda@gmail.com (T.D.); M.R.J.Elsegood@lboro.ac.uk (M.R.J.E.)
5   Department of Physical Chemistry, Faculty of Chemistry, University of Vienna, 1090 Vienna, Austria; jiamin.chin@univie.ac.at
6   Energy Materials Laboratory, School of Chemistry, University of East Anglia, Norwich NR4 7TJ, UK; Oliver.Rowe@gmail.com
*   Correspondence: c.redshaw@hull.ac.uk (C.R.); v.ting@bristol.ac.uk (V.P.T.)

check for updates

Abstract: In this report, we explore the use of supercritical CO_2 (scCO_2) in the synthesis of well-known metal-organic frameworks (MOFs) including Zn-MOF-74 and UiO-66, as well as on the preparation of $[Cu_{24}(OH\text{-}mBDC)_{24}]_n$ metal-organic polyhedra (MOPs) and two new MOF structures $\{[Zn_2(L^1)(DPE)]\cdot 4H_2O\}_n$ and $\{[Zn_3(L^1)_3(4,4'\text{-azopy})]\cdot 7.5H_2O\}_n$, where BTC = benzene-1,3,5-tricarboxylate, BDC = benzene-1,4-dicarboxylate, L^1 = 4-carboxy-phenylene-methyleneamino-4-benzoate, DPE = 1,2-di(4-pyridyl)ethylene, 4.4'-azopy = 4,4'- azopyridine, and compare the results versus traditional solvothermal preparations at low temperatures (i.e., 40 °C). The objective of the work was to see if the same or different products would result from the scCO_2 route versus the solvothermal method. We were interested to see which method produced the highest yield, the cleanest product and what types of morphology resulted. While there was no evidence of additional meso- or macroporosity in these MOFs/MOPs nor any significant improvements in product yields through the addition of scCO_2 to these systems, it was shown that the use of scCO_2 can have an effect on crystallinity, crystal size and morphology.

Keywords: metal-organic framework; supercritical CO_2; crystallisation

1. Introduction

Use of supercritical carbon dioxide (scCO_2) has been extensively studied as a way to incorporate stable permanent porosity in materials during various processing steps including crystallisation [1–3], impregnation [4], dispersion [5], drying [6], and activation [7,8]. The study of porous materials, which can be either ordered structures (including zeolites, metal-organic frameworks (MOFs) and silicates), or disordered materials (including activated carbons, ceramics, metals, and polymers), has been listed among the fastest growing research areas of recent years. In this field, MOFs, normally microporous or mesoporous crystallites constructed by the coordination of transition-metal nodes and organic linkers, have emerged as enabling materials for a wide variety of potential applications, showing promise for

gas storage [9–11], gas separation [12–15], catalysis [16,17], carbon dioxide capture [18–20], and as semiconductors [21,22]. Due to the high interest in these materials, various synthetic methods have been developed beyond the conventional solvothermal approaches which, though a straightforward way to achieve highly crystalline materials, have the potential to use large amounts of organic solvents. In addition, there has been a recent trend towards the creation of multiple porosities (so-called hierarchical pore structures) in these materials [23,24], leading to the development of a number of innovative synthetic strategies including macrostructural templating [25–29], gelation [30–33], acid etching [34–37], use of $scCO_2$ [38–42], and three-dimensional (3D) printing [43–46].

Using $scCO_2$ during the synthesis has been shown to be useful for introducing additional porosity to traditionally microporous or mesoporous MOFs [2,3,47,48]. Unlike other methods such as templating or gelation, using $scCO_2$ can preclude the use of additional purification or activation steps to obtain hierarchical structures without pore collapse. It has been reported that introducing $scCO_2$ into a system containing organic or ionic liquids to obtain a switchable solvent [39] or binary solvent [49,50], can result in additional mesoporosity in MOFs. Interestingly, it has been shown that particle sizes and porosity can also be tuned by varying the CO_2 pressure during synthesis, or by using $scCO_2$ to acid etch MOFs post-synthetically, which introduces a further method for producing hierarchical porous MOFs with improved diffusion rates in catalytic applications [48].

However, the mechanism for the introduction of the larger pores in the MOF crystallites via $scCO_2$ synthesis is not well understood. It was thought that the expanded liquid volume at CO_2 pressure resulted in the mesocellular formation of building blocks before the frameworks were assembled [39]. However, by changing to hydrogen-bonded complexes (using dimethyl sulfoxide (DMSO) instead of dimethylformamide (DMF) to form a precursor solution in HKUST preparation), Doan et al. reported that the formation of the MOF occurred before additional macropores were introduced by $scCO_2$. The latter synthesis can be related to the etching mechanism, which was further studied using different acidic agents [36,37,51]. In addition, use of $scCO_2$ as an anti-solvent (i.e., a solvent in which the crystals are less soluble) to trigger nucleation from a MOF stock solution [47] was shown to remove the need for the 50-times excess of methanol antisolvent used in the original syntheses [52]. Here, we report our investigations into the use of $scCO_2$ in different MOF syntheses to provide information which could improve the understanding and utility of such approaches.

The $scCO_2$ synthetic method which was successfully employed for HKUST-1 [39,47] and Zn-benzene-1,3,5-tricarboxylate (BTC) (in DMF) [38] has here been extended to the Zn-MOF-74, UiO-66 and Zn-BTC (in DMSO) MOF systems, $[Cu_{24}(OH\text{-}mBDC)_{24}]_n$ MOPs, as well as to two new flexible MOF materials $\{[Zn_2(L^1)(DPE)]\cdot 4H_2O\}_n$ and $\{[Zn_3(L^1)_3(4,4'\text{-azopy})]\cdot 7.5H_2O\}_n$. The first four MOF/MOP materials were examined to see the effect of $scCO_2$ on the structure and yield of the products. Zn-BTC was chosen as an example of a HKUST-1 MOF analogue that could not be synthesised using the mixed DMSO and MeOH solvent, which was reported previously as a crucial factor to obtain additional macropores from expanded solvent systems [53], even though this MOF was shown to be a successful candidate for $scCO_2$ templating [38]. $[Cu_{24}(OH\text{-}mBDC)_{24}]_n$ (consisting of metal-organic polyhedral nanocages) was self-assembled from the coordination between copper ions and the angular bifunctional ligand benzene-1,3-dicarboxylate and N,N'-dimethylacetamide, forming a discrete structure [54]. Zn-MOF-74 was also synthesised with $scCO_2$ in the same manner as reported in the literature [47], in order to investigate the behaviour of CO_2 towards different solvent systems. UiO-66 was chosen as an example of a well-known MOF whereby low-temperature syntheses (40 °C) affords gel-like UiO-66 with many defect sites and low crystallinity. We, therefore, sought to investigate if the presence of $scCO_2$ during low-temperature synthesis would improve the crystallinity of the resulting UiO-66. In the syntheses of Zn-Zn-MOF-74, UiO-66, Zn-BTC and the $[Cu_{24}(OH\text{-}mBDC)_{24}]_n$ MOP, $scCO_2$ was introduced to precursor solutions where either MOFs could be formed without additional antisolvents (hereafter referred to as "precursor solution type I") or where the MOFs crystallised only if an antisolvent was added (hereafter referred to as "precursor solution type II"—see

Figure 1). Introducing scCO$_2$ to these different solutions was carried out to help to understand the role of this supercritical fluid in MOF/MOP formation.
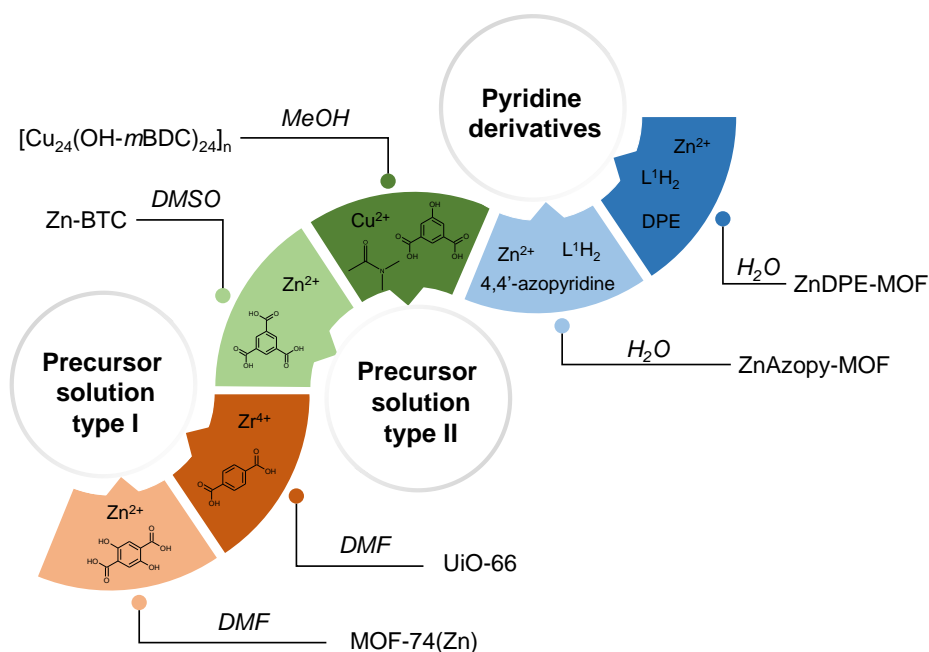
Figure 1. Precursor solutions used to synthesise different metal-organic frameworks/metal-organic polyhedra (MOFs/MOPs) in supercritical CO$_2$ (scCO$_2$). Precursor solution where MOFs/MOPs were formed without additional antisolvents is referred to as "precursor solution type I" and precursor solution where MOFs/MOPs crystallised only in the presence of an antisolvent is referred to as "precursor solution type II".

The two new MOFs made from the flexible reduced Schiff-base linker 4-carboxy-phenylene-methyleneamino-4-benzoic acid (L^{1}H$_2$) and zinc hydroxide ({[Zn$_3$(L^1)$_3$(4,4'-azopy)]·7.5H$_2$O}$_n$—hereafter referred to as ZnAzopy-MOF—and {[Zn$_2$(L^1)(DPE)]·4H$_2$O}$_n$—hereafter called ZnDPE-MOF) were synthesised to see the effect of scCO$_2$ on the crystallisation between transition metals and flexible reduced Schiff-base linkers in the presence of pyridine derivatives as ancillary ligands.

MOF syntheses in scCO$_2$ are normally carried out in the presence of organic liquids such as DMF and DMSO to increase the solubility of both polar and nonpolar compounds in the reaction. It has been shown that using ligands such as *tert*-butylpyridine (*t*-bpy) and 4,4'-bipyridine can increase the solubility of the reagents in the reaction media, resulting in more efficient use of scCO$_2$ [41,42,55]. Here, we employ the flexible reduced Schiff-base compound 4-carboxy-phenylene-methyleneamino-4-benzoic acid as a linker; we note that the biphenyl-4,4'-dicarboxylate linkers have been used with great success in MOF synthesis [56–59].

In addition, research conducted by Yang et al. revealed the variability of structures achievable through the use of the flexible linker (4-carboxy-phenylene-methyleneamino-4-benzoic acid) and the related reduced Schiff-base dicarboxylic acids in conjunction with the flexible neutral pillaring linker 1,4-bis(1*H*-imidazol-1-yl)butane (bbi) and late transition metals [56]. Pillaring linkers, including 1,2-di(4-pyridyl)ethylene (DPE) and 4,4'- azopyridine (4,4'-azopy), were added to build up 2D or 3D MOFs with enhanced uptakes for hydrogen [60,61] and carbon dioxide [62,63]. Thus, we also wanted to investigate whether different crystalline products could be achieved via the use of scCO$_2$ in the synthesis.

2. Materials and Methods

All reagents were purchased from commercial sources and used without further purification. Due to constraints on CO_2 pressure, MOF synthesis at low temperature was preferred. In this study, 40 °C was chosen as the synthesis temperature for Zn-MOF-74, Zn-BTC, $[Cu_{24}(OH-mBDC)_{24}]_n$ metal-organic polyhedron, $\{[Zn_2(L^1)(DPE)]\cdot4H_2O\}_n$ and $\{[Zn_3(L^1)_3(4,4'\text{-azopy})]\cdot7.5H_2O\}_n$. Structures of linkers and pyridine derivatives used in these MOF syntheses are given in Table A1 in Appendix B.4. The conventional syntheses of these materials were also reported to allow comparison with the $scCO_2$ method.

2.1. Synthesis of MOFs by Conventional Methods

2.1.1. Synthesis of Zn-MOF-74

Zn-MOF-74 (i.e., Zn_2(DOBDC), where DOBDC is 2,5-dioxido-1,4-benzenedicarboxylate) was synthesised at low temperature following the method reported by Yaghi et al. [64]. Typically, 0.24 g 2,5-dihydroxyterephthalic acid (H_4DOBDC, 2.4 mmol) and 0.69 g $Zn(OAc)_2\cdot2H_2O$ (6.24 mmol) were dissolved in 40 mL of DMF in a 200 mL glass vial, stirring magnetically for 30 min until a clear solution formed. This vial was sealed with parafilm before being placed in an oven for crystallisation at 40 °C for 24 h. The product was separated by filtration and repeatedly washed with methanol, before drying at room temperature to obtain 0.69 g MOF-74 solid (giving a yield of 34.0% based on Zn). The reaction scheme for formation of this MOF at low temperature is shown in Scheme 1.
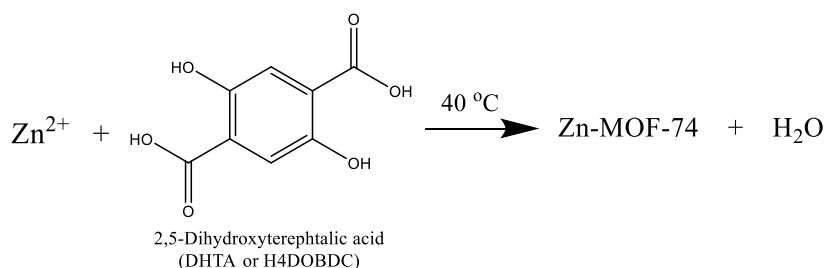

Scheme 1. Synthesis of Zn-MOF-74.

2.1.2. Synthesis of $[Cu_{24}(OH\text{-}mBDC)_{24}]_n$ Metal-Organic Polyhedra

The synthesis of $[Cu_{24}(OH\text{-}mBDC)_{24}]_n$ MOP was followed by the procedure reported for the synthesis of copper-based cuboctahedron metal-organic polyhedra by Lee et al. [65]. The synthesis of this MOF is illustrated in Scheme 2. Typically, 40 mL of 1.46 g OH-*m*BDC in MeOH was mixed with 120 mL of 1.60 g $Cu(OAc)_2\cdot H_2O$ in MeOH (MeOH was used as a solvent in this system) to form a stock solution. No precipitation occurred after 10 days. After that, 12.5 mL *N,N'*-dimethylacetamide and 7.5 mL of MeOH were added to 80 mL of the stock solution, stirring at 200 rpm at 40 °C for 3 days. The blue solid was separated by filtration, repeatedly washed with methanol, yielding 1.9 g of solid after drying at room temperature.
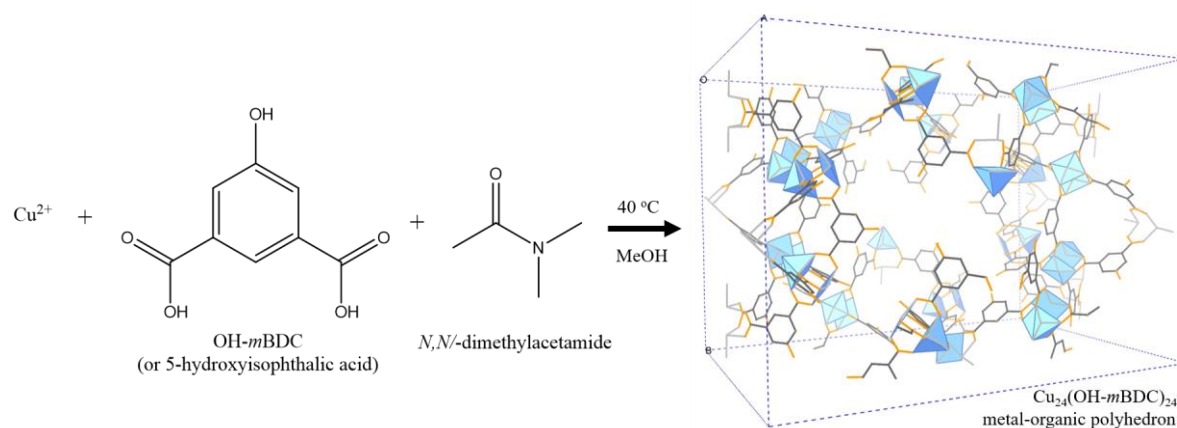
Scheme 2. Synthesis of $[Cu_{24}(OH\text{-}mBDC)_{24}]_n$ (copper clusters represented as blue polyhedra, C–C bonds are represented as dark grey sticks, C–O bonds are represented as orange sticks; all hydrogen atoms are omitted for clarity).

2.1.3. Synthesis of ZnAzopy-MOF

The reduced Schiff-base linker, 4-carboxy-phenylene-methylene-4-benzoic acid (named L^1H_2), was synthesised following the method reported previously by Liu et al. [56]. In brief, 3.0 g 4-carboxybenzoic acid (20 mmol) and 2.7 g 4-aminobenzoic acid (20 mmol) were dissolved in MeOH and the formation of a brownish solid was observed, indicating the formation of the intermediate Schiff-base product. After stirring for 2 h, NaBH$_4$ (2.00 g) was added to reduce the intermediate Schiff-base, resulting in the formation of the intermediate Schiff-base product. The colour faded, and the precipitate dissolved. The solvent was removed from the filtrate by rotary evaporation, and then 100 mL of distilled water was added. The mixture was adjusted to pH ~ 5 with HCl (1.0 mol l^{-1}), and an off-white solid of H_2L^1 formed immediately. The solid was filtered off, washed with Et$_2$O, dried, and recrystallized from MeOH/H$_2$O to afford the diacid, which was used without further purification. The synthetic route for the preparation of this linker is given in Scheme 3.
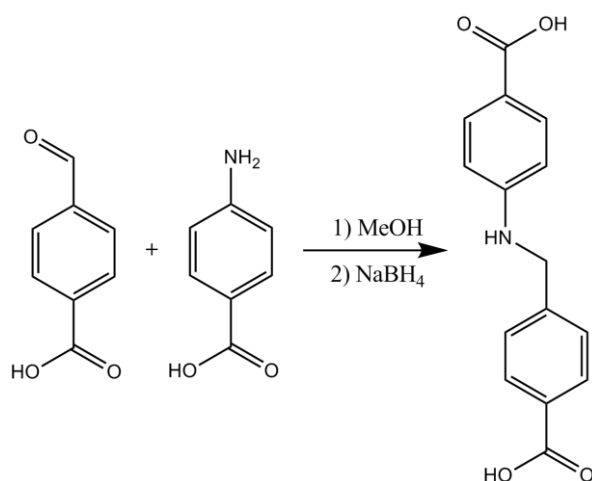
Scheme 3. The synthetic route for the preparation of L^1H_2.

In the synthesis of the ZnAzopy-MOF, 0.1 g of prepared L^1H_2 (0.4 mmol), 0.04 g Zn(OH)$_2$ (0.4 mmol) and 0.04 g 4,4′-azopyridine (0.2 mmol) were added to 20 mL of distilled water. The suspension was sonicated for 10 min., and then transferred to a 23 mL Teflon-lined steel reaction vessel, which was subsequently sealed and heated to 40 °C for 72 h. The product was centrifuged and washed with

distilled water, repeating 3 times, before finally drying at room temperature to obtain 0.06 g of red ZnAzopy-MOF prisms (giving a yield of 37.9% based on Zn).

2.1.4. Synthesis of ZnDPE-MOF

ZnDPE-MOF was synthesised in a similar manner as the ZnAzopy-MOF, but using 1,2-di(4-pyridyl)ethylene (DPE, 0.2 mmol) as a pillaring linker instead of 4,4'-azopyridine. All of the subsequent steps were maintained to obtain 0.14 g of yellow ZnDPE-MOF prisms (giving a yield of 40.6% based on Zn).

2.2. Synthesis of MOFs Using Supercritical CO_2

In the $scCO_2$ routes (Scheme 4), MOF precursor solutions (a mixture of metal salt and acid linker dissolved in a solvent) were produced with the same concentrations as the conventional methods above and were placed in a 200 mL glass vial, then sealed inside a 250 mL cylindrical steel reactor pressure vessel, magnetically stirred at 200 rpm and heated to 40 °C in an oven. The vessel was connected to a $scCO_2$ rig equipped with a flow-controllable liquid pump. The vessel was pressurised to 75 bar at a flowrate of 5 g min^{-1}, keeping the reaction time the same as for the conventional synthesis, i.e., without $scCO_2$. After reaction, the reactor was depressurised slowly to atmospheric pressure. The resulting solution was centrifuged (10,000 rpm for 10 min), washed with methanol 3 times, and dried in air at room temperature to obtain a solid product.

As a comparative control experiment in the absence of $scCO_2$, a mixture of 0.1 g L^1H_2, 0.04 g $Zn(OH)_2$, 0.04 g 1,2-di(4-pyridyl)ethylene and 20 mL distilled water was pressurised with N_2 at 75 bar and 40 °C for 72 h to confirm the effect of the different the gases under supercritical conditions.
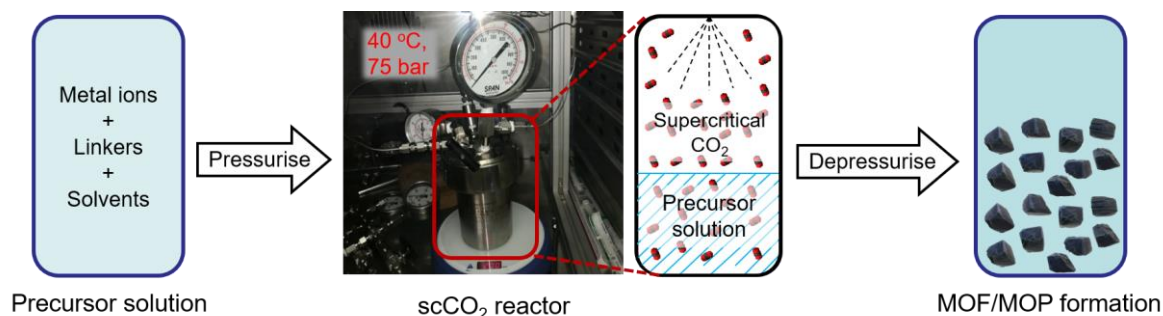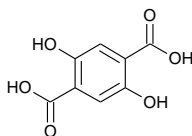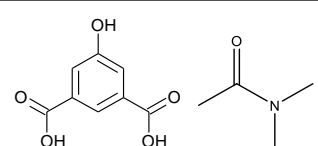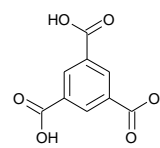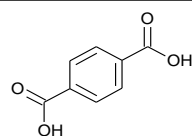

Scheme 4. The $scCO_2$ route employed to synthesise MOFs/MOPs.

3. Results and Discussions

The first part of this study focuses on some well-known MOFs, namely: Zn-MOF-74, UiO-66, Zn-BTC, as well as the $[Cu_{24}(OH\text{-}mBDC)_{24}]_n$ MOP (see Table 1). The second part of this study focuses on new MOF systems (ZnAzopy-MOF and ZnDPE-MOF) using flexible reduced Schiff-base linkers and pyridine derivatives as ancillary ligands.

Synthetic procedures of the well-known MOFs mentioned above with and without $scCO_2$ are given either in the Materials and Methods section or in the Appendix B. In the conventional method in the absence of $scCO_2$, Zn-MOF-74 was synthesised by using DMF and taken to the crystallisation step without the use of antisolvents. Using $scCO_2$ in these MOF syntheses was expected to form the same meso- or macroporous structures as seen in HKUST-1 and Zn-BTC reported by Peng et al. [38,39]. $[Cu_{24}(OH\text{-}mBDC)_{24}]_n$ metal-organic polyhedron with nanoscale polyhedral structure was synthesised in MeOH in which a precursor solution of OH-mBDC and $Cu(OAc)_2$ was formed. The results of these syntheses are further discussed below.

Table 1. Summary of MOFs/MOPs synthesised by conventional methods.

| MOFs	Metal Nodes	Linkers	Comments on the Formation Using Conventional Methods
Zn-MOF-74	Zn		DMF solvent The mixture of Zn^{2+}, H_4DOBDC and DMF is so-called precursor solution type I.
[Cu$_{24}$(OH-*m*BDC)$_{24}$]$_n$ MOP	Cu		MeOH[a] and DMSO[b] solvents This MOF could not be formed in MeOH alone. The mixture of Cu^{2+}, OH-*m*BDC and MeOH is so-called precursor solution type II.
Zn-BTC (see Appendix B.2)	Zn		DMF solvent The mixture of Zn^{2+}, benzene-1,3,5-tricarboxylate (BTC) and DMF is so-called precursor solution type I. This MOF could not be formed from a mixture of DMSO[a] and MeOH[b].
UiO-66 (see Appendix B.3)	Zr		DMF solvent

a: solvent　　　b: antisolvent.

The use of DMSO in BTC to form hydrogen-bonded complexes as reported in the HKUST-1 synthesis [47] was extended to the Zn-BTC. However, this method did not seem to be successful for this MOF, with no precipitation occurring from the stock solution after adding up to ten volume equivalents of MeOH and introducing scCO$_2$ into the system after 3 days. This might be due to the metal–ligand coordination forces between Zn and BTC not being able to overcome the H-bonding, even in the presence of CO$_2$-expanded MeOH as an antisolvent at 40 °C. In the synthesis of UiO-66, 40 °C was chosen as a technically achievable temperature for the scCO$_2$ method. However, UiO-66 synthesised at this temperature via either conventional or scCO$_2$ synthesis, while still crystalline, showed much broader PXRD peaks than normal UiO-66, indicating small crystallite sizes which were not noticeably affected by the presence of scCO$_2$. Syntheses of Zn-BTC (in DMSO) and UiO-66 are described and further discussed in the Appendix B.

3.1. Using scCO$_2$ in Precursor Solution Type I

Zn-MOF-74 was synthesised via the methods given in the Materials and Methods section, enabling comparison of the MOFs synthesised using conventional solvothermal synthesis, without CO$_2$ (here called "normal Zn-MOF-74"), to the MOF synthesised with scCO$_2$ (here called "Zn-MOF-74 in scCO$_2$"). As seen in Figure 2a, normal Zn-MOF-74 samples show a similar powder X-ray diffraction (PXRD) pattern to the simulated Zn-MOF-74 with all the main peaks at 7°, 12°, 22°, 25° and 32° 2θ preserved, confirming that this MOF can be successfully synthesised at low temperature (40 °C), in addition to the higher temperatures of 110 or 100 °C as reported by others [66,67]. The PXRD pattern of Zn-MOF-74 in scCO$_2$ is almost identical to the normal Zn-MOF-74 sample (see Figure 2b), showing that the scCO$_2$ did not overly affect the MOF crystal structure during the synthesis. Yields in both syntheses were also comparable (34% for conventional synthesis and 36% in scCO$_2$). SEM analysis of these samples revealed that the typical morphology of normal Zn-MOF-74 is octahedral with smooth faces, while Zn-MOF-74 in scCO$_2$ shows a similar morphology but with very rough faces (Figure 2b), which might be due to an acidic etching effect of the CO$_2$ at 75 bar and 40 °C for 72 h. Effect of the acid etching

on surface roughness have been previously investigated on amorphous silica and ceramic [68,69]. In addition, etching of MOFs in aqueous acidic solutions such as a mixture of hydroquinone and MeOH (up to 180 °C for 72 h) or a mixture of phosphoric acid, MeOH and DMSO (at 40 °C for up to 10 days) has been shown to result in remarkable effects such as interconnected geometrical macropores and etched hole features [37,51,70].
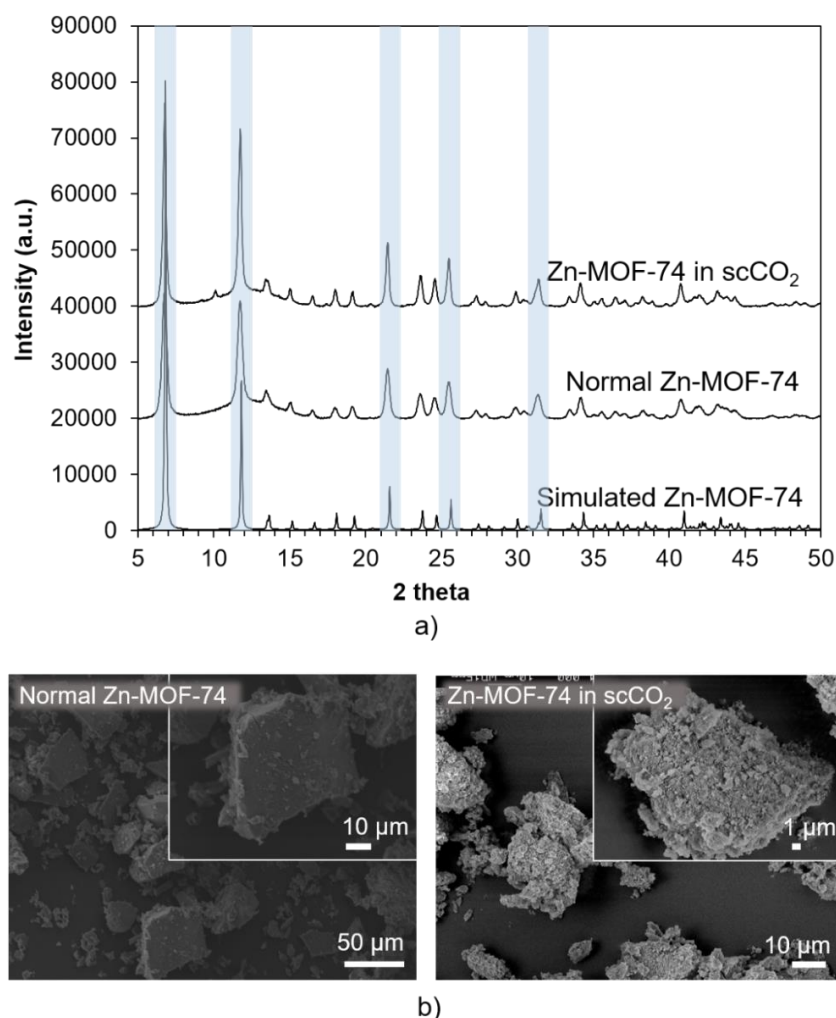
Figure 2. (**a**) PXRD and (**b**) SEM results of normal Zn-MOF-74 and Zn-MOF-74 in scCO$_2$. The main peaks which are preserved (compared to simulated Zn-MOF-74 [71]) are marked by light blue, confirming that this MOF can be successfully synthesised at 40 °C.

Gas sorption experiments (Appendix A) were carried out on these samples to investigate the etching effect on the micro/mesoporosity. The surface area observed in the normal Zn-MOF-74 in this study (BET surface area of normal Zn-MOF-74 is 201 m^2 g^{-1}, see Figure 3a) was lower than those reported in the literature, and the type III isotherm indicated a lower level of microporosity [72]. This may be due to incomplete solvent removal as solvent removal was achieved through scCO$_2$ depressurisation rather than the lengthy high-temperature activation used in previous studies [72]. Further drying these samples under scCO$_2$ flow at 40 °C, 120 bar and 12 h showed improved microporous area (see Appendix C.4). It should be noted that the scCO$_2$ route also provides additional features on the surface of the sample (presumably due to an etching effect), which had the effect of increasing the BET surface area of this MOF (BET surface area of Zn-MOF-74 in scCO$_2$ is ~350 m^2 g^{-1}) compared to the normal Zn-MOF-74 synthesised at low temperature (~200 m^2 g^{-1}, see Figure 3a).

The pore size distributions by the BJH method, however, do not show any significant differences between these two samples, meaning that there were no additional meso- and macropores formed in Zn-MOF-74 through exposure to scCO$_2$, indicating that addition of scCO$_2$ during this MOF synthesis did not help to enlarge the pores as was the case for HKUST-1 [39,47]. Note that the HKUST-1 precursor solution was stabilised by strong O–H ... O hydrogen bonds, forming a two-dimensional supramolecular network within each layer (see Appendix B.1). The donor groups are the hydroxyls of the trimesic acid molecules, while the acceptors are the carbonyl or the sulfoxide O atoms [73].
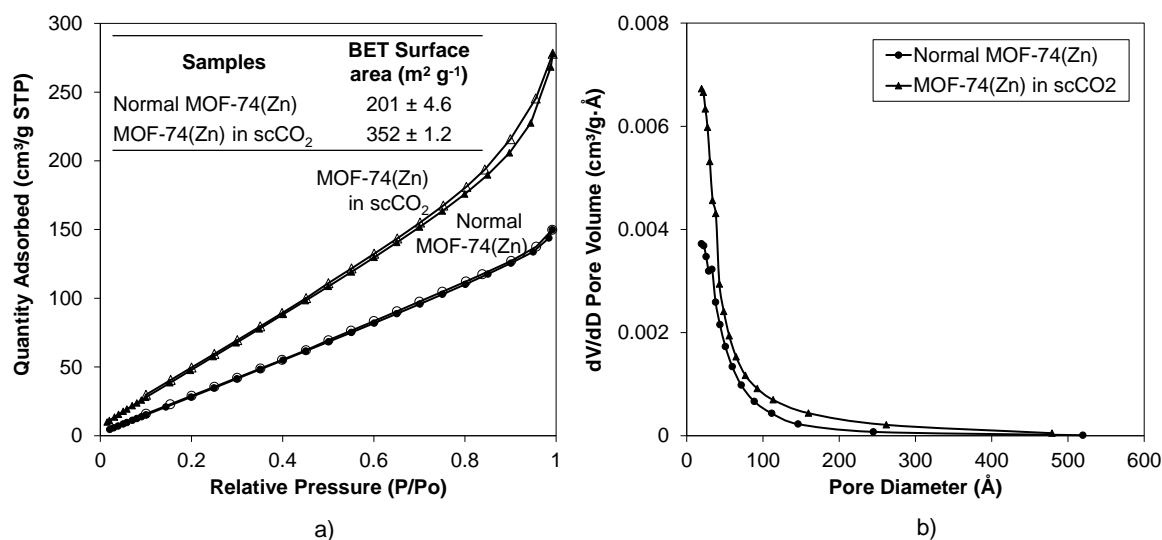

Figure 3. Gas sorption results of normal Zn-MOF-74 and Zn-MOF-74 in scCO$_2$. (**a**) N$_2$ isotherm at 77 K and BET surface area shows that Zn-MOF-74 in scCO$_2$ has improved gas uptake capacity compared with normal Zn-MOF-74. Filled markers are adsorbed N$_2$ and unfilled markers are desorbed N$_2$. (**b**) Pore size distribution by the BJH method shows no additional mesopores in the Zn-MOF-74 synthesised using scCO$_2$.

3.2. Using scCO$_2$ in Precursor Solution Type II

Synthesis of the [Cu$_{24}$(OH-mBDC)$_{24}$]$_n$ MOP is based on self-assembly of Cu$_2$(COO)$_4$ paddlewheels serving as square secondary building units (SBUs) bonded at a 120° angle to OH-mBDC and N,N'-dimethylacetamide serving as the ligands [54]. It was shown that the metal nodes and linkers in this metal-organic polyhedron remained unreacted in MeOH for up to 10 days, resulting in a stable precursor solution before DMSO is introduced. Stable precursors of this sort are promising for investigation of the effect of scCO$_2$ on this metal-organic polyhedron because the aggregation can happen at the same time the solvent is expanded. The crystallinity of [Cu$_{24}$(OH-mBDC)$_{24}$]$_n$ MOP synthesised via the conventional method was confirmed by the similarity between the PXRD pattern of this sample to the simulated pattern reported by Li et al. [74]. In comparing the two [Cu$_{24}$(OH-mBDC)$_{24}$]$_n$ MOP samples synthesised from the same starting materials and at the same temperature but with and without scCO$_2$ pressure (i.e., at 0 and 75 bar), some distortion occurred in the sample treated with scCO$_2$, as evidenced by differences in the intensities and shapes of the PXRD peaks at 6°, 7°, 11°, 14° and 17° 2θ (see Figure 4a). These two samples were analysed under inelastic neutron scattering (INS) spectroscopy (see Appendix C.2), showing that all bond vibrations within these two structures are identical. In the SEM results (Figure 4b), it can be seen that they have identical morphologies. However, the crystallite size of the samples produced in scCO$_2$ is remarkably larger than the conventionally synthesised sample (~2 μm compared with ~1 μm), indicating the scCO$_2$ would lower the deprotonation rate of OH-mBDC, thus decreasing the growth rates of this MOP [75]. Dissolving 1.6 g Cu(OAc)$_2$·H$_2$O and 1.5 g OH-mBDC in 100 mL DMSO resulted in precipitation after 2 h (see Appendix B.1).
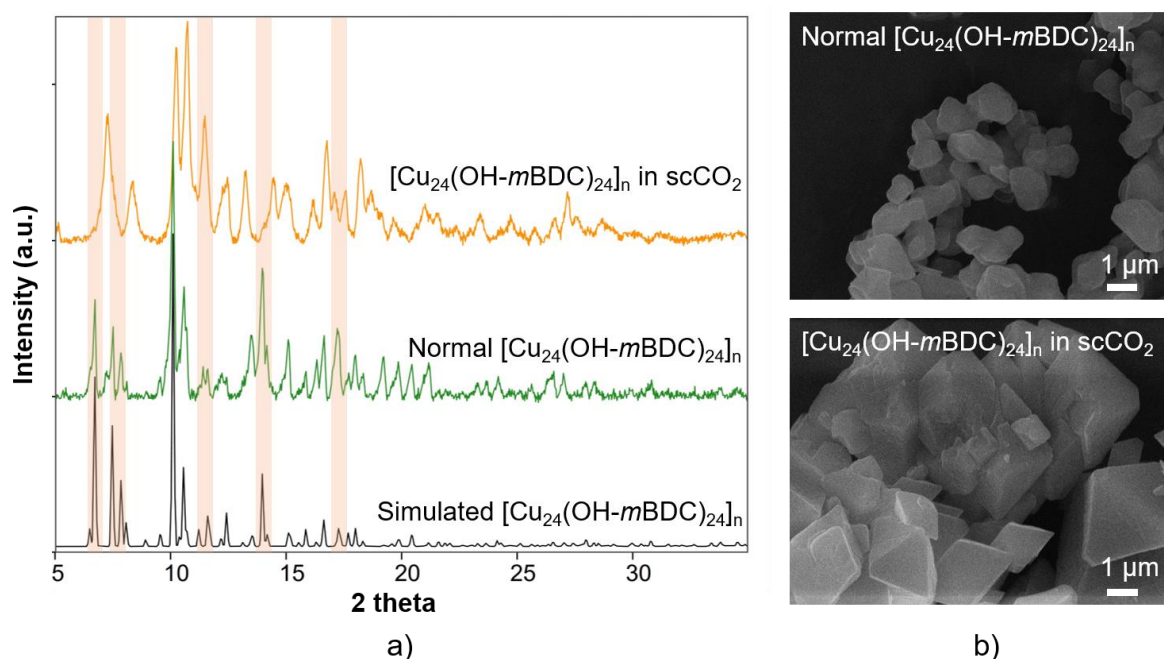
Figure 4. (**a**) PXRD results of simulated $[Cu_{24}(OH\text{-}mBDC)_{24}]_n$, normal $[Cu_{24}(OH\text{-}mBDC)_{24}]_n$ and $[Cu_{24}(OH\text{-}mBDC)_{24}]_n$ in scCO$_2$. Peaks which are changed are marked by light orange. (**b**) SEM results of normal $[Cu_{24}(OH\text{-}mBDC)_{24}]_n$ and $[Cu_{24}(OH\text{-}mBDC)_{24}]_n$ in scCO$_2$, showing that these samples have identical morphology but increased crystal size and do not appear to have additional meso- and macropores.

The results of the syntheses of Zn-MOF-74, UiO-66, $[Cu_{24}(OH\text{-}mBDC)_{24}]_n$ and Zn-BTC (in DMSO) are summarised in Table 2.

Table 2. A summary of the results from both precursor solutions type I and II in the synthesis of MOFs/MOPs in the presence of scCO$_2$.

| Precursor	MOFs	Solvents	Temperature	Comments on the Formation in scCO$_2$
Type I	Zn-MOF-74	DMF	40 °C	Product formed. Crystallinity and morphology preserved. Surface texture changed. Surface area increased.
	UiO-66	DMF	40 °C	Same as without scCO$_2$ at 40 °C but with crystal size smaller than normal UiO-66
Type II	$[Cu_{24}(OH\text{-}mBDC)_{24}]_n$ MOP	MeOH/DMSO	40 °C	Product formed. Crystallinity slightly changed. Morphology preserved. Crystal size increased.
	Zn-BTC (in DMSO)	DMSO	40 °C	Product not formed.

3.3. Using scCO$_2$ in the Presence of Pyridine Derivatives as Ancillary Ligands to Synthesise Pillared MOFs

Synthesis of MOF systems using flexible reduced Schiff base linkers and pyridine derivatives as ancillary ligands, including ZnAzopy-MOF and ZnDPE-MOF were also performed with and without scCO$_2$, to determine the effect of these differing conditions on the nature of the final product.

#### 3.3.1. In ZnAzopy-MOF Synthesis

ZnAzopy-MOF is conventionally synthesised by hydrothermal reaction between the flexible reduced Schiff base linker 4-carboxy-phenylene-methyleneamino-4-benzoic acid (L^{1}H$_2$) and zinc hydroxide and the rigid pillaring linker 4,4'-azopy. The inclusion of an element of rigidity provides a backbone around which the flexible linkers can bind, thereby allowing the assembly of 3D structures bearing novel network topologies. The molecular structure has been determined by single crystal X-ray diffraction (see Figure 5). The asymmetric unit comprises one Zn ion in a general position {Zn(1)}, one Zn ion on a centre of symmetry {Zn(2)}, half the bipyridyl ligand, one and a half dicarboxylate ligands and approx. 3.75 water molecules. Zn(1) is 4-coordinate, severely distorted tetrahedral or triangular based pyramidal, binding to O(1), O(4), O(5'), and N(1), whilst Zn(2) is 6-coordinate, distorted octahedral, binding to six carboxylate oxygens. Three Zn ions form a double lantern arrangement with carboxylates bridging pairs of Zn ions and pyridyl groups capping both ends. The coordination environment around the metal centres in this structure is reminiscent of the paddlewheel SBU, which comprises three zinc centres forming an hour-glass shape by the coordination of carboxylate moieties from six L^1 units in the di-mono-dentate bridging mode in the equatorial positions, with 4,4'-azopy units coordinated to the axial positions of the hour glass, (Figure 5a). The L^1 units extend in six directions in the *a/b* plane, adopting a bent conformation through the rotation of the amine and methylene bridges, whilst the 4,4'-azopy ligands extend along the *c* axis, linking hour-glass SBUs in to an extended 3D framework, bearing roughly cylindrical 1D channels of 4.75 Å diameter observed parallel to the *c* axis (Figure 5b). Elemental analysis of this MOF is given in Appendix C.3, together with alternative views of the structure.


a)　　　　　　　　　　　　　　　　　　　　　　b)
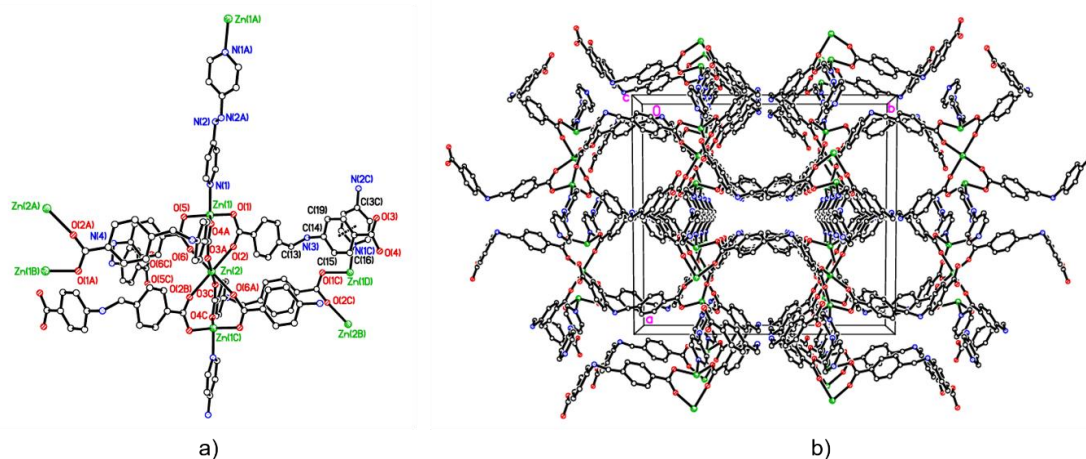
Figure 5. Structure of ZnAzopy-MOF. (**a**) The coordination environment around the Zn^{2+} metal centres in ZnAzopy-MOF. (**b**) Diagram of ZnAzopy-MOF as viewed along the c axis. Carbon, nitrogen, oxygen and zinc atoms are represented by empty, blue, red and green circles, respectively. Hydrogen atoms are omitted for clarity. Selected bond lengths (Å) and angles (°): Zn(1)–N(1) 2.061(8), Zn(1)–O(1) 1.995(8), Zn(1)–O(5) 1.975(6), Zn(2)–O(2) 2.256(12), Zn(2)–O(6) 2.194(10); O(1)–Zn(1)–O(5) 113.5(3), O(1)–Zn(1)–N(1) 96.3(3), O(2)–Zn(2)–O(6) 81.4(4).

This MOF was synthesised without scCO$_2$ ("normal ZnAzopy-MOF") and with scCO$_2$ ("ZnAzopy-MOF in scCO$_2$") using the same concentration of starting materials, reaction temperature and reaction time. It can be seen that the experiment using scCO$_2$ formed a slightly greater yield

than without $scCO_2$ at the same temperature and for the same reaction time (46.7% compared with 37.9%). This might be due to the increased solubility of the metal salt in the mixture of L^1H_2 linker, 4,4′-azopyridine and $scCO_2$. The crystallinity of both samples was examined using PXRD, as shown in Figure 6, with PXRD patterns showing the ZnAzopy-MOF in $scCO_2$ retained the main features (including peaks at 12°, 15°, 18°, 20°, 22°, 23°, 25° and 28° 2θ) when compared to the PXRD patterns of the conventional sample. However, there were some key differences in the pattern of the MOF synthesised in $scCO_2$, including the disappearance of low-angle peaks at 7°, 8° and 13° 2θ, the appearance of a new peak at 17° 2θ and a shift in the peak at 33° 2θ, showing that the addition of $scCO_2$ during the synthesis had a small but noticeable effect on the crystal structure. This might be due to the change in dilution of 4,4′-azopyridine, which was highly soluble in $scCO_2$ [76]. Note that this ancillary ligand is crucial for formation of this MOF. In general, large crystals were precipitated from both syntheses, as can be seen in Figure 7. The increase in the z-dimensional diameter of ZnAzopy-MOF in $scCO_2$ can be referred back to the higher solubility of the reagents in the media with 4,4′-azopyridine used as a co-solvent and a pillaring linker with respect to $scCO_2$, thus supporting crystal growth and nucleation. Gas sorption results (Appendix C.4), however, showed that these samples are non-porous with surface areas less than 20 m^2 g^{-1}.
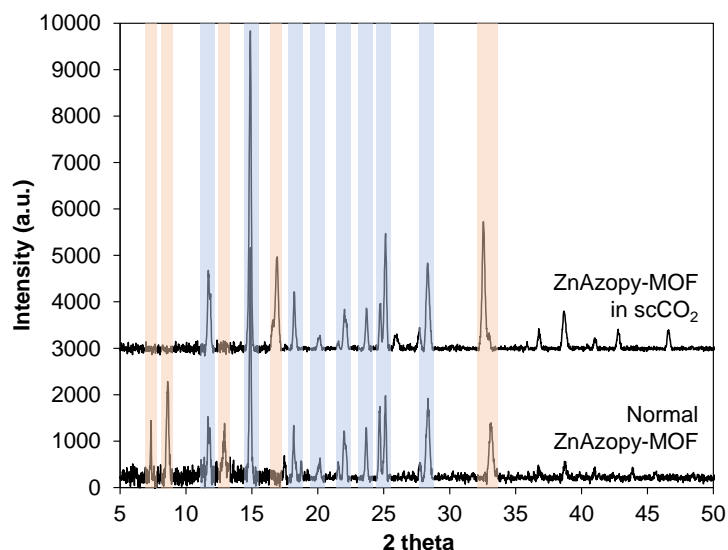

Figure 6. PXRD results of normal ZnAzopy-MOF and ZnAzopy-MOF in $scCO_2$. The main peaks which are preserved are marked by light blue. Peaks which are changed are marked by light orange.
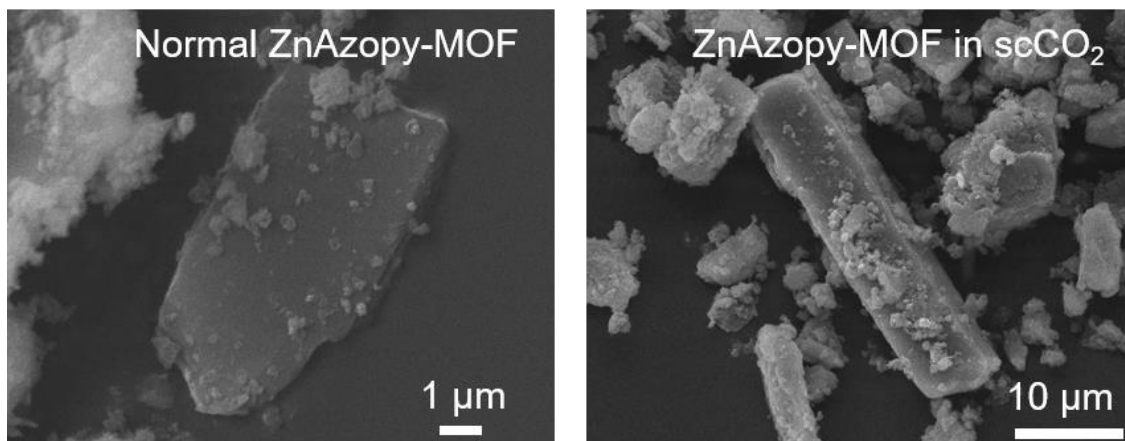
Figure 7. SEM images of normal ZnAzopy-MOF and ZnAzopy-MOF in $scCO_2$.
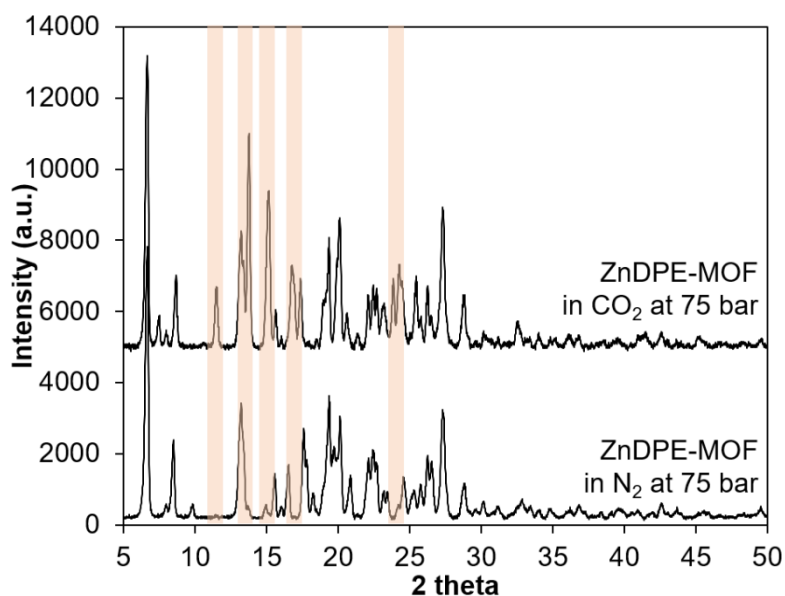
3.3.2. In ZnDPE-MOF Synthesis

ZnDPE-MOF is conventionally formed by the hydrothermal reaction of equimolar quantities of $Zn(OH)_2$ and L^1H_2 with half an equivalent of DPE, to produce the 3D structure$\{[Zn_2(L^1)(DPE)]\cdot4H_2O\}_n$. The coordination environment around the metal centres in this structure, as determined by single crystal X-ray diffraction, is distorted octahedral with two chelating carboxylates and two monodentate DPE pyridinyl nitrogens in a *cis* conformation (see Figure 8a). Coordination of the pyridinyl nitrogens of the neutral DPE linkers in the *cis* conformation gives rise to zig-zag chains and considering also the L^1 connections an overall 3D network (see Figure 8b). Elemental analysis of this MOF is given in the Appendix C.4.


a)　　　　　　　　　　　　　　　　　　　　b)
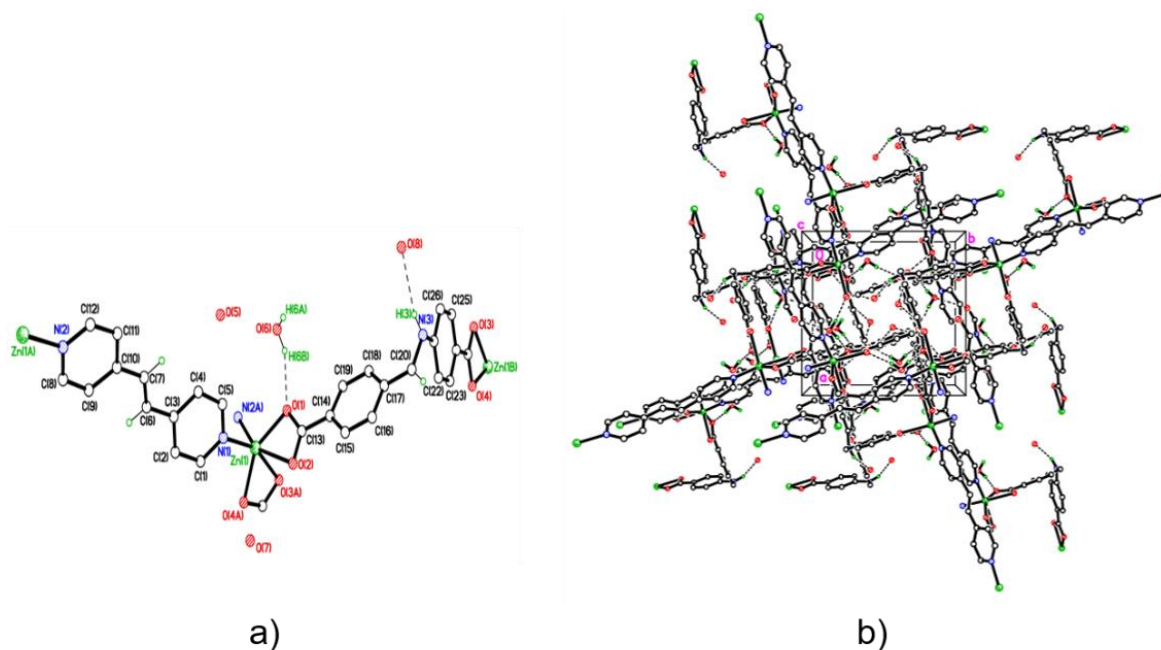
Figure 8. Structure of ZnDPE-MOF. (**a**) The asymmetric unit of ZnDPE-MOF showing the anionic linker and the one unique Zn^{2+} environment; H-bonding interactions as dotted lines. (**b**) Packing plot of ZnDPE-MOF showing the extended structure viewed parallel to c. Carbon, nitrogen, oxygen and zinc atoms are represented by empty circles and blue, red and green circles, respectively. Hydrogen atoms, except those involved in H-bonding, are omitted for clarity. Selected bond lengths (Å) and angles (°): Selected bond lengths (Å) and angles (°): Zn(1)–N(1) 2.062(4), Zn(1)–O(1) 2.038(4), Zn(1)–O(2) 2.434(4), Zn(1)–O(3A) 2.259(3), Zn(1)–O(4A) 2.061(4)), Zn(1)–N(2A) 2.093(4); O(1)–Zn(1)–O(2) 58.28 (14), O(1)–Zn(1)–N(1) 107.34(15), N(2A)–Zn(1)–O(3A) 88.81(14).

Different gases (CO_2 with T_c 31.1 °C and P_c 73.9 bar; and N_2 with T_c −147 °C and P_c 34 bar) were introduced to the precursor solution to synthesise this MOF at 40 °C and 75 bar, forming supercritical systems ($scCO_2$ and scN_2) with increased solubility and decreased polarity. It can be seen that the yield of this MOF in $scCO_2$ is considerably higher than in scN_2 (an increase of 29.8 wt%). The crystallinity of samples was examined using PXRD (see Figure A6 in Appendix C.1 and Figure 9). Most of the main peaks at 8°, 20°, 26°, 27° and 29° 2θ in the simulated ZnDPE-MOF were present in both samples (Figure A6), showing that the crystalline structure had formed and was preserved under high-pressure syntheses. There was a slight difference between the samples synthesised in $scCO_2$ and in scN_2. In the sample synthesised in $scCO_2$, there is an extra peak at 12° 2θ, and the peak appearing at 14° 2θ is more clearly a doublet in comparison to the sample in scN_2. The transformation in peak shape was extended to those at 15°, 17° and 24° 2θ. These differences show the evidence of the effect of CO_2 on the MOF crystal structure. At the same time, the difference in the nature of the supercritical fluids introduced had an effect on the morphology of this MOF during the crystallisation (Figure 10). In general, both

samples appear to not have uniform shape, with the size varying between 3 and 15 μm. However, in more detail, the sample synthesised in scCO$_2$ is represented by bulky crystal agglomerates compared with the smooth surfaces observed for the crystals of the MOF synthesised in N$_2$. This may be due to the etching effect of CO$_2$, which was shown to result in rougher, pitted crystal surfaces in the Zn-MOF-74 synthesis.

Figure 9. PXRD results of ZnDPE-MOF synthesised in scCO$_2$ and scN$_2$ at 40 °C and 75 bar. Peaks which are changed are marked by light orange.
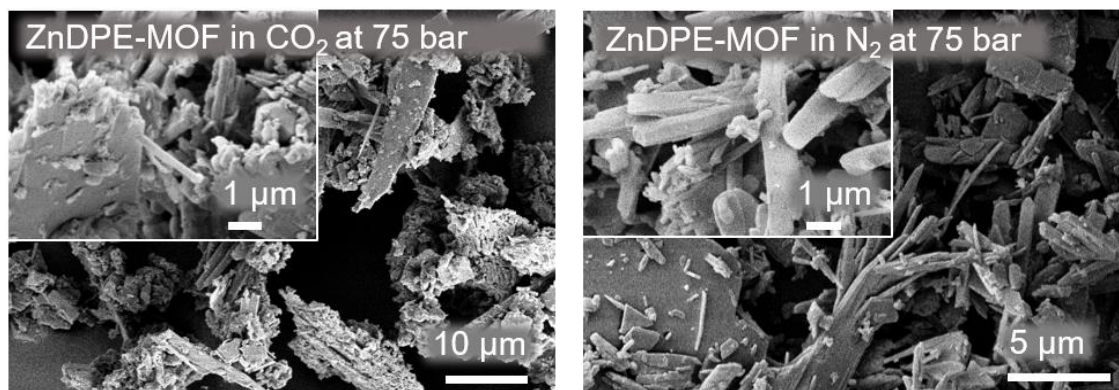
Figure 10. SEM images of ZnDPE-MOF synthesised in scCO$_2$ and scN$_2$ at 75 bar.

4. Conclusions

In this study, scCO$_2$ was introduced to different precursor complexes to synthesise various MOF/MOP systems. There was substantial evidence that scCO$_2$ had an effect on surface texturing and crystal growth in these MOF syntheses. Zn-MOF-74 was formed in scCO$_2$ and precursor solution type I, showing some changes in surface texture and surface area. [Cu$_{24}$(OH-mBDC)$_{24}$]$_n$ MOP with increased crystal size was also formed in scCO$_2$ and precursor solution type II, indicating the growth rates of this MOF increased in the CO$_2$-expanded solvent system. However, there was no evidence showing that additional porosity appeared in these MOFs in scCO$_2$. Zn-BTC (in DMSO) and UiO-66 were formed but contained smaller crystallites in the scCO$_2$ case. The introduction of scCO$_2$ to the synthesis of two new MOF structures {[Zn$_2$(L^1)(DPE)]·4H$_2$O}$_n$ and {[Zn$_3$(L^1)$_3$(4,4′-azopy)]·7.5H$_2$O}$_n$ using pyridine derivatives as ancillary ligands additionally showed that changes in crystallinity and

morphology could result. This was shown (through analogous experiments with N_2 under the same conditions) to be an effect of the presence of $scCO_2$, rather than simply a direct result of high-pressure synthesis. However, again this supercritical fluid did not result in any further meso- or macroporosity in the resulting samples. While $scCO_2$ indeed showed some positive effects on the synthesis of Zn-BTC and HKUST-1 in introducing additional porosity, the mechanism of these effects needs to be further studied to extend the method to other MOF systems.

These findings provide new information on the effects of introducing $scCO_2$ into the synthesis of a broad range of different MOFs, and provides information to direct further application of $scCO_2$ as an approach for morphological control.

Appendix A. Characterisation Methods

Materials after synthesis were tested by powder X-ray diffraction (PXRD) on a BRUKER AXS D8-Advance instrument with Vantec-1 detector using Cu Kα (λ = 1.5418 Å) as the source of X-ray radiation, in flat plate geometry, spinner speed 15 rpm, at 21 °C. The 2θ range, between 2–60° was used with a 0.02° interval for collection and 20 min scans.

Scanning electron microscopy (SEM) images were taken using JEOL IT300 SEM with a SED detector at School of Chemistry, University of Bristol with the following settings, objective apeture: 1, acceleration voltage: 5 kV, probe current: 10.3 m, working distance: 10.8 mm and magnifications from 350 to 40,000 times. The samples were coated with 15 nm silver before conducting the experiment.

Gas sorption isotherms were determined using nitrogen sorption at 77 K with a Micromeritics 3-Flex volumetric gas sorption analysis system (nitrogen with purity of 99.9999% was purchased from Air Products). Samples were degassed at 120 °C under dynamic high vacuum (10^{-6} mbar) over 6 h prior to analysis. The total pore volume was taken at the end of the filling of the pore. Surface area was determined by the BET method according to British Standards, with relative pressure (P/P$_o$) selected considering the Rouquerol consistency criterion between values of 0 and 0.3.

Single crystal diffraction data for ZnAzopy-MOF and ZnDPE-MOF were collected on a Rigaku Saturn 724+ CCD diffractometer using a rotating anode X-ray source and 10 cm confocal mirrors monochromator at 100 K. Data were corrected for absorption and Lp effects. Structures were solved by direct methods and refined by full-matrix least squares on F^2 [77]. Further details are given in Table 1. H atoms were included in a constrained riding model except for those on water where coordinates were refined. In ZnAzopy-MOF the badly disordered solvent water in the void spaces was modelled as diffuse electron density by the Platon Squeeze procedure which recovered 2×73 and 2×78 electrons over four voids in the unit cell [78]. This equates to approx. 30 water molecules per unit cell or approx. 7.5 per void or Zn_3 unit. The CH_2NH linkers C(13)/N(3) and C(28)/N(4) in the dicarboxylate ligands could not be clearly distinguished and were each modelled as 50/50 C/N. For ZnAzopy-MOF, where disorder was modelled, restraints on both geometry and displacement parameters were applied. CCDC 935555 and 1919724 contain the supplementary crystallographic data for this paper. These data can be obtained free of charge from The Cambridge Crystallographic Data Centre via www.ccdc.cam.ac.uk/data_request/cif.

Analysis of [Cu$_{24}$(OH-mBDC)$_{24}$]$_n$ MOP with inelastic neutron scattering (INS) spectroscopy was achieved on the TOSCA indirect geometry spectrometer at ISIS Neutron and Muon Source, Didcot, UK [79]. The dehydrated sample was prepared within a glove box under an inert argon atmosphere. The sample was first loaded into aluminium foil sachets, with the loaded sample mass recorded. The sachets were then sealed between two aluminium plates, using indium wire as a seal to keep the sample under an inert atmosphere. INS spectra were recorded within the energy transfer range −80–8050 cm^{-1}, at a temperature of 10 K for 5–7 h. Subsequent data analysis, visualisation and normalisation was achieved using the Mantid software [80].

Appendix B. Additional Syntheses and Discussion

Appendix B.1. Synthesis of [Cu$_{24}$(OH-mBDC)$_{24}$]$_n$ Metal-Organic Polyhedron in DMSO and MeOH

Figure A1. A mixture of 1.6 g Cu(OAc)$_2$·H$_2$O and 1.5 g OH-mBDC in 100 mL DMSO after 2 h, showing a precipitation occurred in [Cu$_{24}$(OH-mBDC)$_{24}$]$_n$ stock solution.
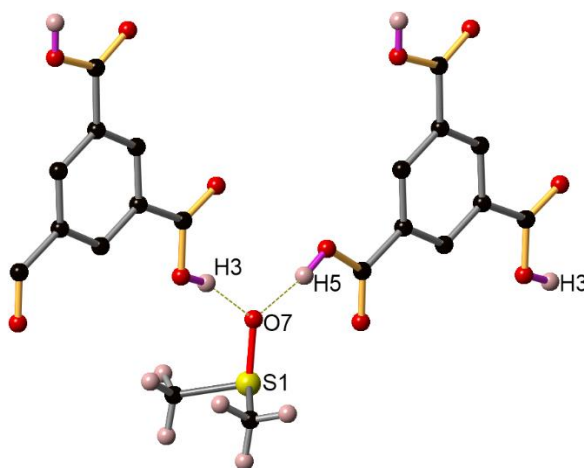
Figure A2. Hydrogen bonds formed between trimesic acid and DMSO. C atoms are represented by back spheres. O atoms are represented by red spheres. H atoms are represented by pink spheres. S atoms are represented by yellow spheres.

Appendix B.2. Synthesis of Zn-BTC in DMSO and MeOH

The coordination of Zn(II) metal nodes and benzene-1,3,5-tricarboxylic acid (BTC) linkers, resulting in a 3D open network as found in Zn-BTC MOF. This MOF was successfully synthesised by

solvothermal reactions between BTC and $Zn(NO_3)_2 \cdot 6H_2O$ in a mixture of DMF and DMAC without any additives [81]. In fact, Peng et al. used this MOF to test the effect of CO_2 in the presence of N-EtFOSA/TMGT solution [38]. By changing the pressure of the formed ionic liquid system from 10 to 63 bar, tetrahedron-like Zn-BTC particles with some evidence of mesopores were observed. In some cases where a high number of bulky molecules get involved, macropores were more favoured to minimise diffusion barrier, hence were managed to achieve in this study. With the success of the creation of macroporous HKUST-1 (or Cu-BTC) in $scCO_2$ [47], Zn-BTC synthesis was repeated in the same manner. In a typical experiment, 3.1 mg $Zn(NO_3)_2 \cdot 6H_2O$ (10 mmol) and 1.5 mg BTC (5 mmol) were dissolved in 100 mL DMSO, resulting a clear precursor solution. As demonstrated previously [82], H-bonding between DMSO and BTC dominated the metal-ligand coordination forces and hindered the aggregation process, resulting in a stable stock solution. This solution (1–5 mL) was added in MeOH at varied volume ratio between 1:1 and 1:10, and left for up to 10 days at 40 °C. However, no precipitation was observed, consistent with the precursor solution of HKUST-1 [47]. A mixture of 4 mL stock solution and 40 mL MeOH was pressurised with CO_2 at 40 °C and 75 bar; however, no solid was formed after 3 days. This might be due to the metal–ligand coordination forces between Zn and BTC not being able to overcome the H-bonding even in the presence of CO_2-expanded MeOH as an antisolvent at 40 °C.
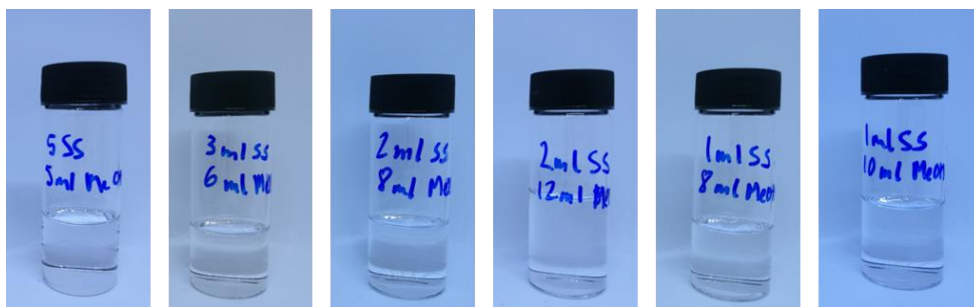
Figure A3. Stock solution of $Zn(NO_3)_2 \cdot 6H_2O$ (10 mmol), BTC (5 mmol) and DMSO in MeOH at different volume ratios. Stock solution/MeOH volume ratio (from left to right) is 1:1, 1:2, 1:4, 1:6, 1:8 and 1:10.

Appendix B.3. Synthesis of UiO-66 in DMF at Low Temperature

Normal UiO-66 was synthesised by dissolving 3.18 g $ZrCl_4$ (0.014 mol) and 2.04 g benzene-1,4-dicarboxylic acid (H_2BDC) (0.014 mol) in 80 mL anhydrous dimethylformamide (DMF) at room temperature. The reaction of this step is given in Scheme A1. The reaction mixture was heated in an autoclave at 120 °C for 24 h. After cooling in air to room temperature the white solid was separated by filtration, repeatedly washed with DMF and dried at room temperature. In the modified synthetic procedure, the autoclave was heated at 40 °C instead of 120 °C, with all other steps remaining the same. In the synthesis with $scCO_2$, the stock solution was added in a glass vial and placed in a 250 mL cylindrical steel reactor pressure vessel and heated to 40 °C in an oven. The vessel was connected to a $scCO_2$ rig equipped with a flow controllable liquid pump. The vessel was pressurised to 75 bar at a flowrate of 5 g min^{-1} for 24 h. After that, the reactor was depressurised slowly to atmospheric pressure. The white solid was separated by filtration, repeatedly washed with DMF and dried at room temperature.
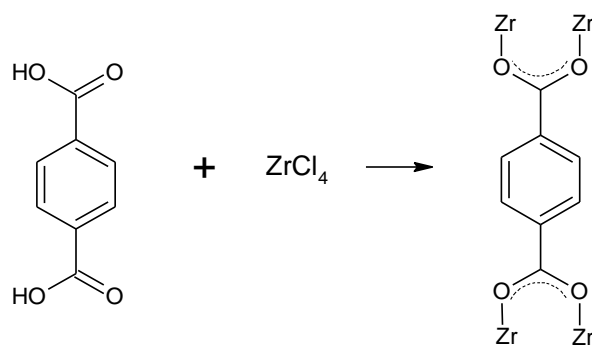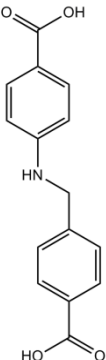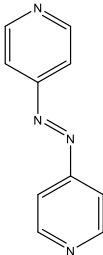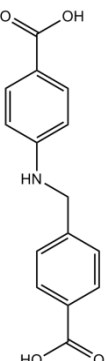
Scheme A1. Synthesis of UiO-66.
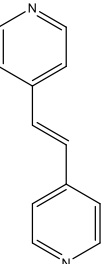
The sample synthesised at 40 °C and dried at room temperature appeared to be gel-like light yellow crystals which are very different from the solids in the sample synthesised at 120 °C. Tian et al. also reported that a gel like UiO-66 monolith could be formed by a sol-gel process and mild drying conditions [83]. In the PXRD results, it can be seen that the low temperature synthesised sample has preserved peaks at 7°, 12°, 22°, 26°, 31°, 43° and 50° 2θ (see Figure A4), confirming the UiO-66 structure in this sample. However, these peaks appeared much broader than the peaks in normal UiO-66, showing that the sample synthesised at 40 °C has smaller crystallite size than those synthesised at 120 °C. It has been demonstrated that UiO-66 obtained by room-temperature synthesis had defect sites with the maximal number achieved (~1.3 missing linker per SBU) at a temperature of 45 °C [84]. In this study, highly-crystalline MOFs were the principal focus. The scCO$_2$ experiment was applied in this MOF synthesis, however, the PXRD patterns of both samples synthesised at 40 °C are almost identical, showing that scCO$_2$ did not enhance the crystallite size in this MOF.
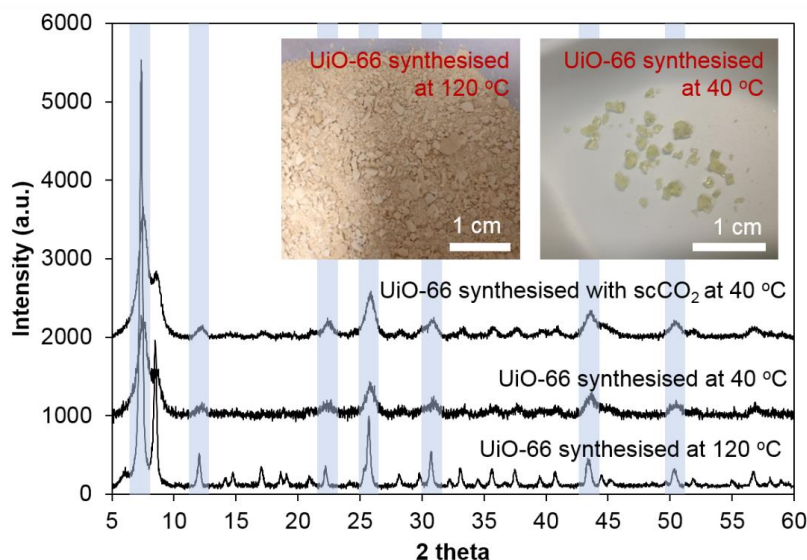
Figure A4. UiO-66 synthesised at 40 °C (with and without scCO$_2$) and 120 °C.

Appendix B.4. Summary of MOFs Synthesised in the Presence of Pyridine Derivatives

Table A1. Reagents used for the synthesis of MOFs with pyridine derivatives.

MOFs	Metal Nodes	Linkers	Pyridine Derivatives
ZnAzopy-MOF	Zn	L^1H_2	4,4′-azopyridine
ZnDPE-MOF	Zn	L^1H_2	1,2-di(4-pyridyl)ethylene

Appendix C. Additional Results of MOFs Synthesised in the Presence of Pyridine Derivatives

Appendix C.1. PXRD Results
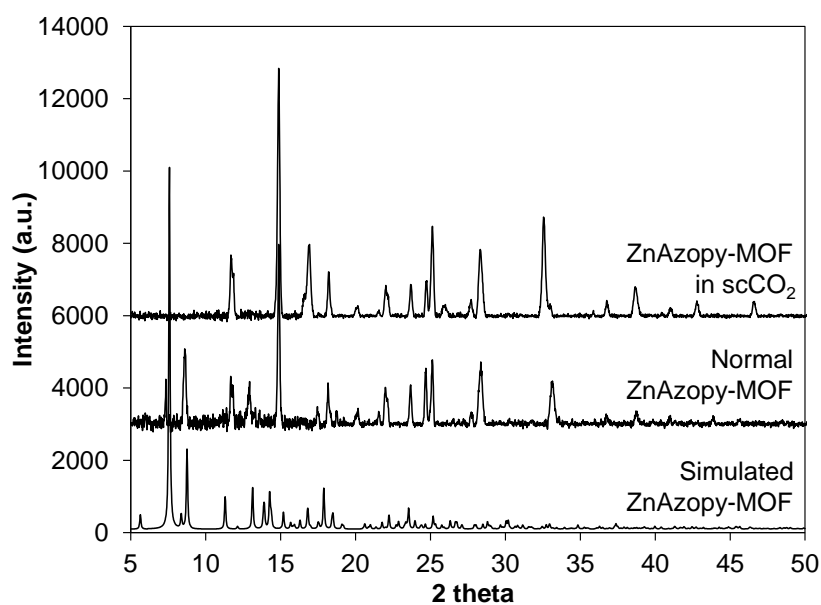
Figure A5. PXRD results of simulated ZnAzopy-MOF, normal ZnAzopy-MOF and ZnAzopy-MOF in scCO$_2$.
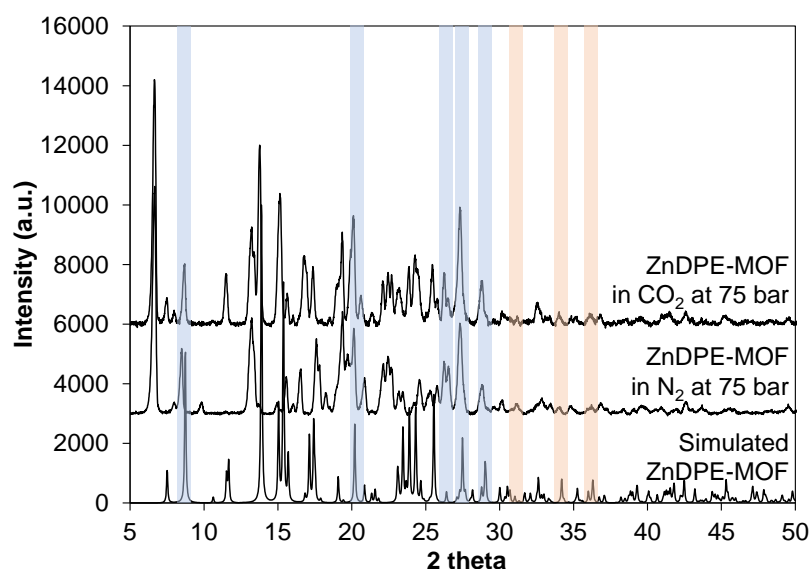
Figure A6. PXRD results of ZnDPE-MOF synthesised in scCO$_2$ and N$_2$ at 40 °C and 75 bar compared with simulated ZnDPE-MOF, showing that the primary crystallinity was maintained in the prepared samples (highlighted by light blue). Peaks for ZnO are highlighted by light orange, showing that residual ZnO from synthesised samples are insignificant.

Appendix C.2. INS Results
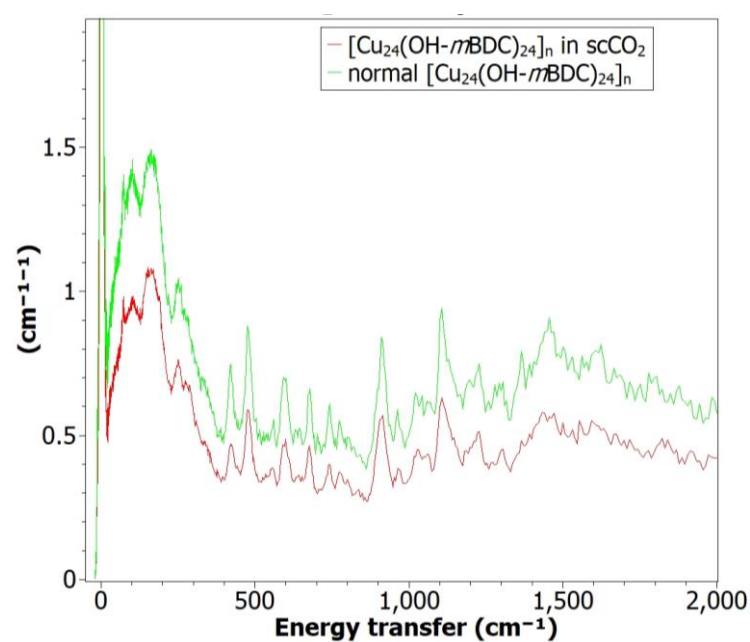
Figure A7. INS spectra of normal [Cu$_{24}$(OH-*m*BDC)$_{24}$]$_n$ and [Cu$_{24}$(OH-*m*BDC)$_{24}$]$_n$ in scCO$_2$, showing bond vibrations within two structures are identical.

Appendix C.3. Method and Elemental Analysis of ZnAzopy-MOF and ZnDPE-MOF

Ligand **L**^{1}H$_2$ (0.2 mmol, 0.05 g), Zn(OH)$_2$ (0.2 mmol, 0.02 g) and 4,4′-azopy (0.1 mmol, 0.02 g) were added to 10 mL distilled water. The suspension was transferred to a 23 mL Teflon-lined steel reaction vessel which was subsequently sealed and heated to 110 °C for 72 h. The vessel was then cooled at a rate of 2 °C h^{-1} to room temperature, yielding 0.04 g red prisms (50.5% based on Zn). Elem. anal. calcd. for ZnAzopy-MOF (C$_{55}$H$_{41}$N$_7$O$_{12}$Zn$_3$·7H$_2$O): C 50.26; H 4.22; N 7.46; found C 50.61; H

4.29; N 7.08%: IR/cm^{-1} (KBr): 3348(w), 2717(w), 2667(w), 2359(w), 2336(w), 1700(w), 1653(w), 1606(s), 1559(w), 1539(w), 1519(w), 1506(w), 1488(w), 1331(m), 1281(m), 1222(w), 1180(m), 1142(w), 1111(w), 1080(w), 1046(w), 1029(w), 1018(w), 987(w), 847(m), 782(m), 761(m), 721(w),703(w).

Ligand **L**^{1}H$_2$ (0.2 mmol, 0.05 g), Zn(OH)$_2$ (0.2 mmol, 0.02 g), DPE (0.1 mmol, 0.018 g) and one drop of 6 M of NaOH solution were added to 10 mL distilled water. The suspension was then transferred to a 23 mL Teflon-lined steel reaction vessel which was subsequently sealed and heated to 110 °C for 72 h. The vessel was then cooled at a rate of 6 °C h^{-1} to room temperature, yielding 0.045 g yellow prisms (68.9% based on Zn). Elem. anal. calcd. for ZnDPE-MOF (C$_{27}$H$_{26}$N$_3$O$_7$Zn$_2$): C 51.05; H 4.12; N 6.61; found C 51.25, H 4.06, N 6.50. IR/cm^{-1}: 3325(b), 2971(w), 2942(w), 1738(m), 1610(s), 1544(m), 1524(w), 1511(w), 1387(s), 1366(m), 1283(w), 1277(w), 1227(w), 1217(w), 1205(w), 1181(m), 1139(w), 1087(w), 1063(w), 1024(m), 966(w), 955(w), 862(m), 844(m), 833(m), 786(s), 763(s), 706(m), 644(w), 636(m), 628(m).

Table A2. Crystallographic data for structures ZnAzopy-MOF and ZnDPE-MOF.

Structure	*ZnAzopy-MOF*	*ZnDPE-MOF*
Formula	C$_{55}$H$_{41}$N$_7$O$_{12}$Zn$_3$·7.5H$_2$O	C$_{27}$H$_{20}$N$_3$O$_4$Zn$_2$·4(H$_2$O)
Formula weight (g mol^{-1})	1323.17	653.31
Crystal system	Monoclinic	Tetragonal
Space group	*C*2/*c*	*P*4$_1$
Unit cell dimensions		
a (Å)	21.2518(17)	11.76800(19)
b (Å)	23.3115(18)	
c (Å)	12.3700(9)	19.8120(5)
α (°)	90	90
β (°)	96.612(7)	90
γ (°)	90	90
V (Å^3)	6087.5(8)	2743.68(11)
Z	4	4
Calculated density (Mgm^{-3})	1.444	1.423
Absorption coefficient (mm^{-1})	1.25	0.95
Transmission factors (max, min)	0.907, 0.963	1.00, 0.74
Crystal size (mm^3)	0.08 × 0.05 × 0.03	0.06 × 0.05 × 0.03
θ_{max} (°)	22.5	27.5
Reflections measured	9389	14455
Unique reflections	3860	5757
R_{int}	0.053	0.032
Reflections with $F^2 > 2\sigma(F^2)$	2201	5040
Number of parameters	349	362
R_1, wR_2 [$F^2 > 2\sigma(F^2)$]	0.108, 0.321	0.043, 0.103
GOOF	1.07	1.03
Largest difference peak and hole (e Å^{-3})	0.86 and −2.11	0.32 and −0.45

a)

b)

c)

d)
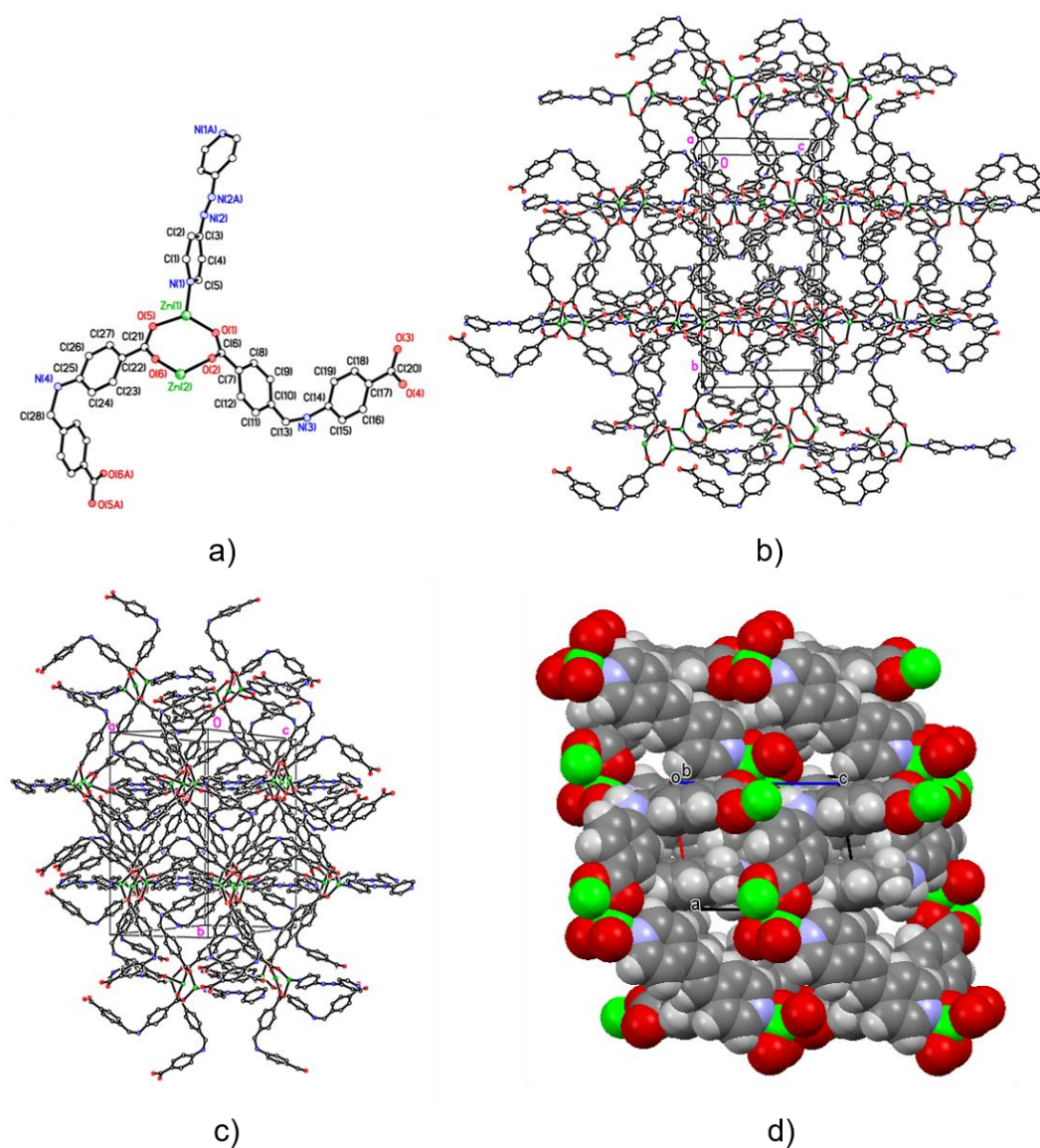
Figure A8. Alternative models and views of ZnAzopy-MOF: ball and stick models in asymmetric unit (**a**) and packing plot (**b**,**c**), and space filling model (**d**). Carbon, nitrogen, oxygen and zinc atoms are represented by empty circles and blue, red and green circles, respectively. Selected bond lengths (Å) and angles (°): Zn(1)–N(1) 2.061(8), Zn(1)–O(1) 1.995(8), Zn(1)–O(5) 1.975(6), Zn(2)–O(2) 2.256(12), Zn(2)–O(6) 2.194(10); O(1)–Zn(1)–O(5) 113.5(3), O(1)–Zn(1)–N(1) 96.3(3), O(2)–Zn(2)–O(6) 81.4(4).

a)

b)

c)
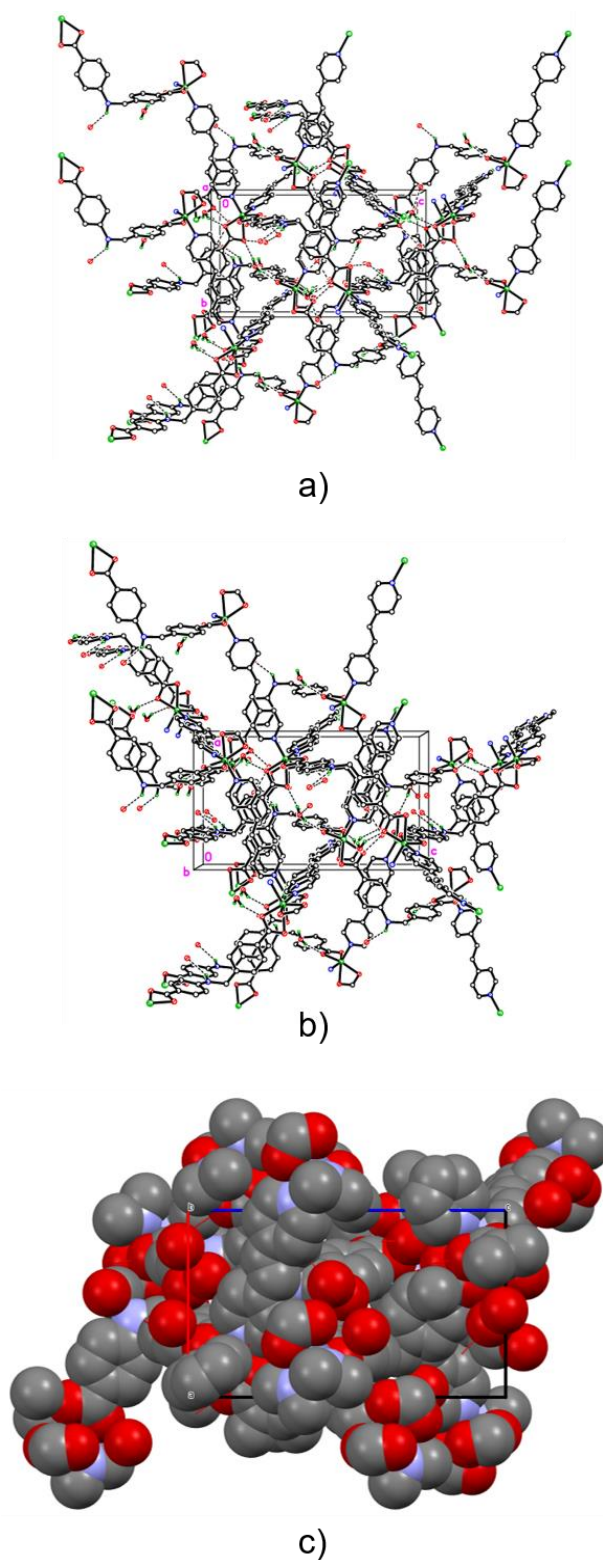
Figure A9. Alternative models of ZnDPE-MOF: ball and stick models in packing plot (**a**,**b**), and space filling model (**c**). Carbon, nitrogen, oxygen and zinc atoms are represented by empty circles and blue, red and green circles, respectively. Selected bond lengths (Å) and angles (°): Selected bond lengths (Å) and angles (°): Zn(1)–N(1) 2.062(4), Zn(1)–O(1) 2.038(4), Zn(1)–O(2) 2.434(4), Zn(1)–O(3A) 2.259(3), Zn(1)–O(4A) 2.061(4)), Zn(1)–N(2A) 2.093(4); O(1)–Zn(1)–O(2) 58.28 (14), O(1)–Zn(1)–N(1) 107.34(15), N(2A)–Zn(1)–O(3A) 88.81(14).

Appendix C.4. Gas Sorption Results of ZnAzopy-MOF
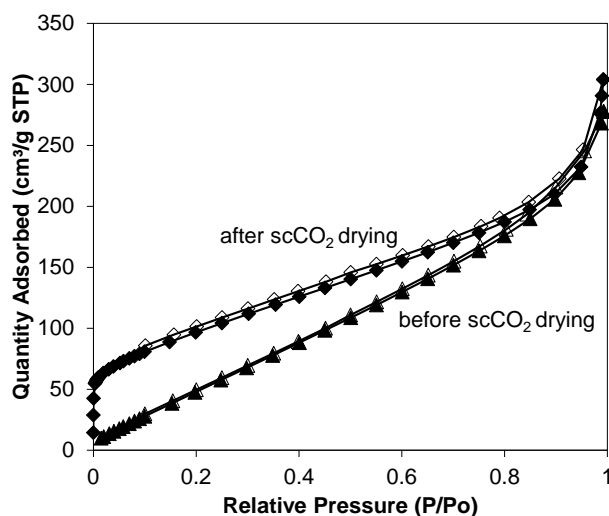
Figure A10. 77 K nitrogen isotherms of Zn-MOF-74 in $scCO_2$ before and after dried with $scCO_2$ flow at 40 °C, 120 bar and 12 h.

a)

b)
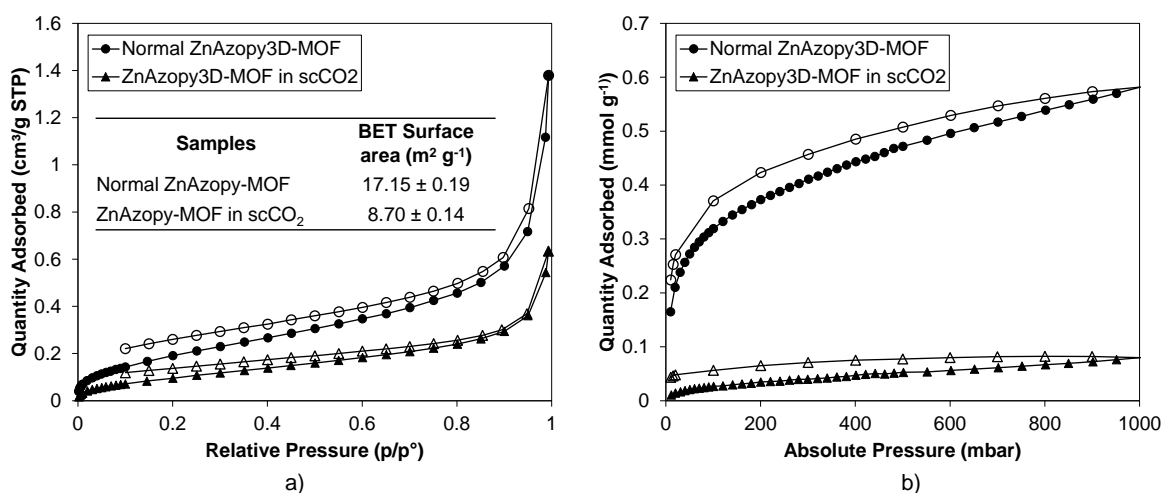
Figure A11. Gas sorption results of ZnAzopy-MOF synthesised without $scCO_2$ (normal ZnAzopy-MOF) and with $scCO_2$ (ZnAzopy-MOF in $scCO_2$). (**a**) N_2 isotherm and BET surface area. (**b**) CO_2 isotherm. Filled markers are adsorbed gas molecules and unfilled markers are desorbed gas molecules.

References

1. Liu, C.; Zhang, B.; Zhang, J.; Peng, L.; Kang, X.; Han, B.; Wu, T.; Sang, X.; Ma, X. Gas promotes the crystallization of nano-sized metal-organic frameworks in ionic liquid. *Chem. Commun.* **2015**, *51*, 11445–11448. [CrossRef]
2. López-Periago, A.; López-Domínguez, P.; Pérez Barrio, J.; Tobias, G.; Domingo, C. Binary supercritical CO_2 solvent mixtures for the synthesis of 3D metal-organic frameworks. *Microporous Mesoporous Mater.* **2016**, *234*, 155–161. [CrossRef]
3. Portolés-Gil, N.; Lanza, A.; Aliaga-Alcalde, N.; Ayllón, J.A.; Gemmi, M.; Mugnaioli, E.; López-Periago, A.M.; Domingo, C. Crystalline Curcumin bioMOF Obtained by Precipitation in Supercritical CO_2 and Structural Determination by Electron Diffraction Tomography. *ACS Sustain. Chem. Eng.* **2018**, *6*, 12309–12319. [CrossRef]
4. Weidner, E. Impregnation via supercritical CO_2–What we know and what we need to know. *J. Supercrit. Fluids* **2018**, *134*, 220–227. [CrossRef]

5. Zhao, Y.; Zhang, J.; Song, J.; Li, J.; Liu, J.; Wu, T.; Zhang, P.; Han, B. Ru nanoparticles immobilized on metal-organic framework nanorods by supercritical CO_2-methanol solution: Highly efficient catalyst. *Green Chem.* **2011**, *13*, 2078–2082. [CrossRef]

6. Cooper, A.I.; Rosseinsky, M.J. Metal-organic frameworks: Improving pore performance. *Nat. Chem.* **2009**, *1*, 26–27. [CrossRef] [PubMed]

7. Nelson, A.P.; Farha, O.K.; Mulfort, K.L.; Hupp, J.T. Supercritical processing as a route to high internal surface areas and permanent microporosity in metal-organic framework materials. *J. Am. Chem. Soc.* **2009**, *131*, 458–460. [CrossRef] [PubMed]

8. Farha, O.K.; Hupp, J.T. Rational design, synthesis, purification, and activation of metal-organic framework materials. *Acc. Chem. Res.* **2010**, *43*, 1166–1175. [CrossRef] [PubMed]

9. Gómez-Gualdrón, D.A.; Colón, Y.J.; Zhang, X.; Wang, T.C.; Chen, Y.S.; Hupp, J.T.; Yildirim, T.; Farha, O.K.; Zhang, J.; Snurr, R.Q. Evaluating topologically diverse metal-organic frameworks for cryo-adsorbed hydrogen storage. *Energy Environ. Sci.* **2016**, *9*, 3279–3289. [CrossRef]

10. Mason, J.A.; Oktawiec, J.; Taylor, M.K.; Hudson, M.R.; Rodriguez, J.; Bachman, J.E.; Gonzalez, M.I.; Cervellino, A.; Guagliardi, A.; Brown, C.M.; et al. Methane storage in flexible metal-organic frameworks with intrinsic thermal management. *Nature* **2015**, *527*, 357–361. [CrossRef]

11. Zou, L.; Zhou, H.C. Hydrogen storage in metal-organic frameworks. *Nanostruct. Mater. Next Gener. Energy Storage Convers. Hydrog. Prod. Storage Util.* **2017**, *112*, 143–170.

12. Holcroft, J.M.; Hartlieb, K.J.; Moghadam, P.Z.; Bell, J.G.; Barin, G.; Ferris, D.P.; Bloch, E.D.; Algaradah, M.M.; Nassar, M.S.; Botros, Y.Y.; et al. Carbohydrate-mediated purification of petrochemicals. *J. Am. Chem. Soc.* **2015**, *137*, 5706–5719. [CrossRef] [PubMed]

13. Li, J.R.; Kuppler, R.J.; Zhou, H.C. Selective gas adsorption and separation in metal-organic frameworks. *Chem. Soc. Rev.* **2009**, *38*, 1477–1504. [CrossRef] [PubMed]

14. Decoste, J.B.; Peterson, G.W. Metal-organic frameworks for air purification of toxic chemicals. *Chem. Rev.* **2014**, *114*, 5695–5727. [CrossRef] [PubMed]

15. Zhao, X.; Wang, Y.; Li, D.S.; Bu, X.; Feng, P. Metal–Organic Frameworks for Separation. *Adv. Mater.* **2018**, *30*, 869–932. [CrossRef] [PubMed]

16. Liu, J.; Chen, L.; Cui, H.; Zhang, J.; Zhang, L.; Su, C.Y. Applications of metal-organic frameworks in heterogeneous supramolecular catalysis. *Chem. Soc. Rev.* **2014**, *43*, 6011–6061. [CrossRef]

17. Wu, C. De Crystal Engineering of Metal-Organic Frameworks for Heterogeneous Catalysis. *Sel. Nanocatal. Nanosci. Concepts Heterog. Homog. Catal.* **2011**, *110*, 271–298.

18. Sumida, K.; Rogow, D.L.; Mason, J.A.; McDonald, T.M.; Bloch, E.D.; Herm, Z.R.; Bae, T.H.; Long, J.R. Carbon dioxide capture in metal-organic frameworks. *Chem. Rev.* **2012**, *112*, 724–781. [CrossRef]

19. McDonald, T.M.; Mason, J.A.; Kong, X.; Bloch, E.D.; Gygi, D.; Dani, A.; Crocellà, V.; Giordanino, F.; Odoh, S.O.; Drisdell, W.S.; et al. Cooperative insertion of CO_2 in diamine-appended metal-organic frameworks. *Nature* **2015**, *519*, 303–308. [CrossRef]

20. Yazaydin, A.Ö.; Snurr, R.Q.; Park, T.H.; Koh, K.; Liu, J.; LeVan, M.D.; Benin, A.I.; Jakubczak, P.; Lanuza, M.; Galloway, D.B.; et al. Screening of metal-organic frameworks for carbon dioxide capture from flue gas using a combined experimental and modeling approach. *J. Am. Chem. Soc.* **2009**, *131*, 18198–18199. [CrossRef]

21. Férey, G. Hybrid porous solids: Past, present, future. *Chem. Soc. Rev.* **2008**, *37*, 191–214. [CrossRef] [PubMed]

22. Sheberla, D.; Sun, L.; Blood-Forsythe, M.A.; Er, S.; Wade, C.R.; Brozek, C.K.; Aspuru-Guzik, A.; Dincă, M. High electrical conductivity in Ni_3(2,3,6,7,10,11- hexaiminotriphenylene)$_2$, a semiconducting metal-organic graphene analogue. *J. Am. Chem. Soc.* **2014**, *136*, 8859–8862. [CrossRef] [PubMed]

23. Guan, H.Y.; LeBlanc, R.J.; Xie, S.Y.; Yue, Y. Recent progress in the syntheses of mesoporous metal–organic framework materials. *Coord. Chem. Rev.* **2018**, *369*, 76–90. [CrossRef]

24. Doan, H.V.; Amer Hamzah, H.; Karikkethu Prabhakaran, P.; Petrillo, C.; Ting, V.P. Hierarchical Metal–Organic Frameworks with Macroporosity: Synthesis, Achievements, and Challenges. *Nano Micro Lett.* **2019**, *11*, 54. [CrossRef]

25. Granato, T.; Testa, F.; Olivo, R. Catalytic activity of HKUST-1 coated on ceramic foam. *Microporous Mesoporous Mater.* **2012**, *153*, 236–246. [CrossRef]

26. Sandra, F.; Depardieu, M.; Mouline, Z.; Vignoles, G.L.; Iwamoto, Y.; Miele, P.; Backov, R.; Bernard, S. Polymer-Derived Silicoboron Carbonitride Foams for CO_2 Capture: From Design to Application as Scaffolds for the in Situ Growth of Metal-Organic Frameworks. *Chem. A Eur. J.* **2016**, *22*, 8346–8357. [CrossRef]

27. Betke, U.; Proemmel, S.; Eggebrecht, J.G.; Rannabauer, S.; Lieb, A.; Scheffler, M.; Scheffler, F. Micro-Macroporous Composite Materials: SiC Ceramic Foams Functionalized with the Metal Organic Framework HKUST-1. *Chem. Ing. Tech.* **2016**, *88*, 264–273. [CrossRef]

28. Betke, U.; Proemmel, S.; Rannabauer, S.; Lieb, A.; Scheffler, M.; Scheffler, F. Silane functionalized open-celled ceramic foams as support structure in metal organic framework composite materials. *Microporous Mesoporous Mater.* **2017**, *239*, 209–220. [CrossRef]

29. Betke, U.; Klaus, M.; Eggebrecht, J.G.; Scheffler, M.; Lieb, A. MOFs meet macropores: Dynamic direct crystallization of the microporous aluminum isophthalate CAU-10 on reticulated open-cellular alumina foams. *Microporous Mesoporous Mater.* **2018**, *265*, 43–56. [CrossRef]

30. Moitra, N.; Fukumoto, S.; Reboul, J.; Sumida, K.; Zhu, Y.; Nakanishi, K.; Furukawa, S.; Kitagawa, S.; Kanamori, K. Mechanically stable, hierarchically porous $Cu_3(btc)_2$ (HKUST-1) monoliths via direct conversion of copper(ii) hydroxide-based monoliths. *Chem. Commun.* **2015**, *51*, 3511–3514. [CrossRef]

31. Bo, S.; Ren, W.; Lei, C.; Xie, Y.; Cai, Y.; Wang, S.; Gao, J.; Ni, Q.; Yao, J. Flexible and porous cellulose aerogels/zeolitic imidazolate framework (ZIF-8) hybrids for adsorption removal of Cr(IV) from water. *J. Solid State Chem.* **2018**, *262*, 135–141. [CrossRef]

32. Ren, W.; Gao, J.; Lei, C.; Xie, Y.; Cai, Y.; Ni, Q.; Yao, J. Recyclable metal-organic framework/cellulose aerogels for activating peroxymonosulfate to degrade organic pollutants. *Chem. Eng. J.* **2018**, *349*, 766–774. [CrossRef]

33. Zhang, Y.; Cai, J.; Zhang, D.; Ke, X.; Zhang, L. Shaping metal-organic framework materials with a honeycomb internal structure. *Chem. Commun.* **2018**, *54*, 3775–3778. [CrossRef] [PubMed]

34. Cai, G.; Jiang, H.L. A Modulator-Induced Defect-Formation Strategy to Hierarchically Porous Metal–Organic Frameworks with High Stability. *Angew. Chem. Int. Ed.* **2017**, *56*, 563–567. [CrossRef]

35. Hu, M.; Ju, Y.; Liang, K.; Suma, T.; Cui, J.; Caruso, F. Void Engineering in Metal–Organic Frameworks via Synergistic Etching and Surface Functionalization. *Adv. Funct. Mater.* **2016**, *26*, 5827–5834. [CrossRef]

36. Koo, J.; Hwang, I.C.; Yu, X.; Saha, S.; Kim, Y.; Kim, K. Hollowing out MOFs: Hierarchical micro- and mesoporous MOFs with tailorable porosity via selective acid etching. *Chem. Sci.* **2017**, *8*, 6799–6803. [CrossRef]

37. Ahmed, A.; Hodgson, N.; Barrow, M.; Clowes, R.; Robertson, C.M.; Steiner, A.; McKeown, P.; Bradshaw, D.; Myers, P.; Zhang, H. Macroporous metal-organic framework microparticles with improved liquid phase separation. *J. Mater. Chem. A* **2014**, *2*, 9085–9090. [CrossRef]

38. Peng, L.; Zhang, J.; Li, J.; Han, B.; Xue, Z.; Zhang, B.; Shi, J.; Yang, G. Hollow metal-organic framework polyhedra synthesized by a CO_2-ionic liquid interfacial templating route. *J. Colloid Interface Sci.* **2014**, *416*, 198–204. [CrossRef]

39. Peng, L.; Zhang, J.; Xue, Z.; Han, B.; Sang, X.; Liu, C.; Yang, G. Highly mesoporous metal-organic framework assembled in a switchable solvent. *Nat. Commun.* **2014**, *5*, 933–969. [CrossRef]

40. López-Domínguez, P.; López-Periago, A.M.; Fernández-Porras, F.J.; Fraile, J.; Tobias, G.; Domingo, C. Supercritical CO_2 for the synthesis of nanometric ZIF-8 and loading with hyperbranched aminopolymers. Applications in CO_2 capture. *J. CO_2 Util.* **2017**, *18*, 147–155.

41. López-Periago, A.M.; Portoles-Gil, N.; López-Domínguez, P.; Fraile, J.; Saurina, J.; Aliaga-Alcalde, N.; Tobias, G.; Ayllón, J.A.; Domingo, C. Metal-Organic Frameworks Precipitated by Reactive Crystallization in Supercritical CO_2. *Cryst. Growth Des.* **2017**, *17*, 2864–2872. [CrossRef]

42. Portolés-Gil, N.; Gowing, S.; Vallcorba, O.; Domingo, C.; López-Periago, A.M.; Ayllón, J.A. Supercritical CO_2 utilization for the crystallization of 2D metal-organic frameworks using tert-butylpyridine additive. *J. CO_2 Util.* **2018**, *24*, 444–453.

43. Thakkar, H.; Eastman, S.; Al-Naddaf, Q.; Rownaghi, A.A.; Rezaei, F. 3D-Printed Metal-Organic Framework Monoliths for Gas Adsorption Processes. *ACS Appl. Mater. Interfaces* **2017**, *9*, 35908–35916. [CrossRef] [PubMed]

44. Young, A.J.; Guillet-Nicolas, R.; Marshall, E.S.; Kleitz, F.; Goodhand, A.J.; Glanville, L.B.L.; Reithofer, M.R.; Chin, J.M. Direct ink writing of catalytically active UiO-66 polymer composites. *Chem. Commun.* **2019**, *55*, 2190–2193. [CrossRef] [PubMed]

45. Evans, K.A.; Kennedy, Z.C.; Arey, B.W.; Christ, J.F.; Schaef, H.T.; Nune, S.K.; Erikson, R.L. Chemically Active, Porous 3D-Printed Thermoplastic Composites. *ACS Appl. Mater. Interfaces* **2018**, *10*, 15112–15121. [CrossRef] [PubMed]

46. Sultan, S.; Abdelhamid, H.N.; Zou, X.; Mathew, A.P. CelloMOF: Nanocellulose Enabled 3D Printing of Metal–Organic Frameworks. *Adv. Funct. Mater.* **2019**, *29*, 1805372. [CrossRef]

47. Doan, H.V.; Fang, Y.; Yao, B.; Dong, Z.; White, T.J.; Sartbaeva, A.; Hintermair, U.; Ting, V.P. Controlled Formation of Hierarchical Metal-Organic Frameworks Using CO_2-Expanded Solvent Systems. *ACS Sustain. Chem. Eng.* **2017**, *5*, 7887–7893. [CrossRef]

48. Doan, H.; Madapusi, S.; Chiang, K.; Pattisson, S.; Taylor, S.H.; Ting, V. Novel Hierarchical Copper-Based Metal-Organic Frameworks for Improved Catalytic Performance. 2019. Available online: https://chemrxiv.org/articles/Novel_Hierarchical_Copper-Based_Metal-Organic_Frameworks_for_Improved_Catalytic_Performance/9699863 (accessed on 31 December 2019).

49. Zhao, Y.; Zhang, J.; Han, B.; Song, J.; Li, J.; Wang, Q. Metal-organic framework nanospheres with well-ordered mesopores synthesized in an ionic liquid/CO_2/surfactant system. *Angew. Chem. Int. Ed.* **2011**, *50*, 636–639. [CrossRef]

50. Yu, H.; Xu, D.; Xu, Q. Dual template effect of supercritical CO_2 in ionic liquid to fabricate a highly mesoporous cobalt metal-organic framework. *Chem. Commun.* **2015**, *51*, 13197–13200. [CrossRef]

51. Doan, H.V.; Sartbaeva, A.; Eloi, J.C.; Davis, S.; Ting, V.P. Defective hierarchical porous copper-based metal-organic frameworks synthesised via facile acid etching strategy. *Sci. Rep.* **2019**, *9*, 10887. [CrossRef]

52. Zhuang, J.L.; Ceglarek, D.; Pethuraj, S.; Terfort, A. Rapid room-temperature synthesis of metal-organic framework HKUST-1 crystals in bulk and as oriented and patterned thin films. *Adv. Funct. Mater.* **2011**, *21*, 1442–1447. [CrossRef]

53. Dodson, R.A.; Wong-Foy, A.G.; Matzger, A.J. The Metal-Organic Framework Collapse Continuum: Insights from Two-Dimensional Powder X-ray Diffraction. *Chem. Mater.* **2018**, *30*, 6559–6565. [CrossRef]

54. Abourahma, H.; Coleman, A.W.; Moulton, B.; Rather, B.; Shahgaldian, P.; Zaworotko, M.J. Hydroxylated nanoballs: Synthesis, crystal structure, solubility and crystallization on surfaces. *Chem. Commun.* **2001**, *22*, 2380–2381. [CrossRef] [PubMed]

55. López-Periago, A.; Vallcorba, O.; Frontera, C.; Domingo, C.; Ayllón, J.A. Exploring a novel preparation method of 1D metal organic frameworks based on supercritical CO_2. *Dalt. Trans.* **2015**, *44*, 7548–7553. [CrossRef] [PubMed]

56. Liu, Y.Y.; Wang, Z.H.; Yang, J.; Liu, B.; Liu, Y.Y.; Ma, J.F. A series of coordination polymers based on reduced Schiff base multidentate anions and bis(imidazole) ligands: Syntheses, structures and photoluminescence. *CrystEngComm* **2011**, *13*, 3811–3821. [CrossRef]

57. Marshall, R.J.; Lennon, C.T.; Tao, A.; Senn, H.M.; Wilson, C.; Fairen-Jimenez, D.; Forgan, R.S. Controlling interpenetration through linker conformation in the modulated synthesis of Sc metal-organic frameworks. *J. Mater. Chem. A* **2018**, *6*, 1181–1187. [CrossRef]

58. Wang, Y.; Bredenkötter, B.; Rieger, B.; Volkmer, D. Two-dimensional metal–organic frameworks (MOFs) constructed from heterotrinuclear coordination units and 4,4′-biphenyldicarboxylate ligands. *J. Chem. Soc. Dalt. Trans.* **2006**, *6*, 689–696. [CrossRef]

59. Kalmutzki, M.J.; Hanikel, N.; Yaghi, O.M. Secondary building units as the turning point in the development of the reticular chemistry of MOFs. *Sci. Adv.* **2018**, *4*, eaat9180. [CrossRef]

60. Wang, H.N.; Meng, X.; Qin, C.; Wang, X.L.; Yang, G.S.; Su, Z.M. A series of pillar-layer metal-organic frameworks based on 5-aminoisophthalic acid and 4,4′-bipyridine. *Dalt. Trans.* **2012**, *41*, 1047–1053. [CrossRef]

61. Chang, Z.; Zhang, D.S.; Chen, Q.; Li, R.F.; Hu, T.L.; Bu, X.H. Rational construction of 3D pillared metal-organic frameworks: Synthesis, structures, and hydrogen adsorption properties. *Inorg. Chem.* **2011**, *50*, 7555–7562. [CrossRef]

62. Xuan, Z.H.; Zhang, D.S.; Chang, Z.; Hu, T.L.; Bu, X.H. Targeted structure modulation of "pillar-layered" metal-organic frameworks for CO_2 capture. *Inorg. Chem.* **2014**, *53*, 8985–8990. [CrossRef] [PubMed]

63. Chen, C.; Jia, M.; Wang, G.; Li, X.; Li, S. High and selective CO_2 uptake in a nitrogen-rich pillar-layered metal organic framework. *RSC Adv.* **2015**, *5*, 104932–104935. [CrossRef]

64. Tranchemontagne, D.J.; Hunt, J.R.; Yaghi, O.M. Room temperature synthesis of metal-organic frameworks: MOF-5, MOF-74, MOF-177, MOF-199, and IRMOF-0. *Tetrahedron* **2008**, *64*, 8553–8557. [CrossRef]

65. Lee, J.; Kwak, J.H.; Choe, W. Evolution of form in metal-organic frameworks. *Nat. Commun.* **2017**, *8*, 14070. [CrossRef] [PubMed]

66. Grant Glover, T.; Peterson, G.W.; Schindler, B.J.; Britt, D.; Yaghi, O. MOF-74 building unit has a direct impact on toxic gas adsorption. *Chem. Eng. Sci.* **2011**, *66*, 163–170. [CrossRef]

67. Rowsell, J.L.C.; Yaghi, O.M. Effects of functionalization, catenation, and variation of the metal oxide and organic linking units on the low-pressure hydrogen adsorption properties of metal-organic frameworks. *J. Am. Chem. Soc.* **2006**, *128*, 1304–1315. [CrossRef]

68. Affatigato, M.; Osborne, D.H.; Haglund, R.F. Effect of Surface Roughness on the Acid Etching of Amorphous Silica. *J. Am. Ceram. Soc.* **2005**, *79*, 688–694. [CrossRef]

69. Zogheib, L.V.; Della Bona, A.; Kimpara, E.T.; Mccabe, J.F. Effect of hydrofluoric acid etching duration on the roughness and flexural strength of a lithium disilicate-based glass ceramic. *Braz. Dent. J.* **2011**, *22*, 45–50. [CrossRef]

70. Yoo, Y.; Jeong, H.K. Generation of covalently functionalized hierarchical IRMOF-3 by post-synthetic modification. *Chem. Eng. J.* **2012**, *181–182*, 740–745. [CrossRef]

71. Rosi, N.L.; Kim, J.; Eddaoudi, M.; Chen, B.; O'Keeffe, M.; Yaghi, O.M. Rod packings and metal-organic frameworks constructed from rod-shaped secondary building units. *J. Am. Chem. Soc.* **2005**, *127*, 1504–1518. [CrossRef]

72. Garzón-Tovar, L.; Carné-Sánchez, A.; Carbonell, C.; Imaz, I.; Maspoch, D. Optimised room temperature, water-based synthesis of CPO-27-M metal-organic frameworks with high space-time yields. *J. Mater. Chem. A* **2015**, *3*, 20819–20826. [CrossRef] [PubMed]

73. Berns, S.; Hernández, G.; Portillo, R.; Gutiérrez, R. Trimesic acid dimethyl sulfoxide solvate: Space group revision. *Acta Crystallogr. Sect. E Struct. Rep. Online* **2008**, *64*, o1366. [CrossRef] [PubMed]

74. Li, J.R.; Zhou, H.C. Bridging-ligand-substitution strategy for the preparation of metalg-organic polyhedra. *Nat. Chem.* **2010**, *2*, 893–898. [CrossRef]

75. Wang, F.; Guo, H.; Chai, Y.; Li, Y.; Liu, C. The controlled regulation of morphology and size of HKUST-1 by "coordination modulation method". *Microporous Mesoporous Mater.* **2013**, *173*, 181–188. [CrossRef]

76. Yan, J.; Zheng, L.J.; Du, B.; Qian, Y.F.; Ye, F. Dye solubility in supercritical carbon dioxide fluid. *Therm. Sci.* **2015**, *19*, 1311–1315. [CrossRef]

77. Sheldrick, G.M. Crystal structure refinement with SHELXL. *Acta Crystallogr. Sect. C Struct. Chem.* **2015**, *71*, 3–8. [CrossRef]

78. Hendle, J.; Badger, J. A code of standards: Validation of protein structures in the era of structural genomics. *Acta Crystallogr. Sect. A Found. Crystallogr.* **2002**, *58*, c58. [CrossRef]

79. Pinna, R.S.; Rudić, S.; Parker, S.F.; Armstrong, J.; Zanetti, M.; Škoro, G.; Waller, S.P.; Zacek, D.; Smith, C.A.; Capstick, M.J.; et al. The neutron guide upgrade of the TOSCA spectrometer. *Nucl. Instrum. Methods Phys. Res. Sect. A* **2018**, *896*, 68–74. [CrossRef]

80. Arnold, O.; Bilheux, J.C.; Borreguero, J.M.; Buts, A.; Campbell, S.I.; Chapon, L.; Doucet, M.; Draper, N.; Ferraz Leal, R.; Gigg, M.A.; et al. Mantid—Data analysis and visualization package for neutron scattering and μSR experiments. *Nucl. Instrum. Methods Phys. Res. Sect. A* **2014**, *764*, 156–166. [CrossRef]

81. Huang, X.; Chen, Y.; Lin, Z.; Ren, X.; Song, Y.; Xu, Z.; Dong, X.; Li, X.; Hu, C.; Wang, B. Zn-BTC MOFs with active metal sites synthesized via a structure-directing approach for highly efficient carbon conversion. *Chem. Commun.* **2014**, *50*, 2624–2627. [CrossRef]

82. Ameloot, R.; Cobechiya, E.; Uji-i, H.; Martens, J.A.; Hofkens, J.; Alaerts, L.; Sels, B.F.; De Vos, D.E. Direct patterning of oriented metal-organic framework crystals via control over crystallization kinetics in clear precursor solutions. *Adv. Mater.* **2010**, *22*, 2685–2688. [CrossRef] [PubMed]

83. Tian, T.; Zeng, Z.; Vulpe, D.; Casco, M.E.; Divitini, G.; Midgley, P.A.; Silvestre-Albero, J.; Tan, J.C.; Moghadam, P.Z.; Fairen-Jimenez, D. A sol-gel monolithic metal-organic framework with enhanced methane uptake. *Nat. Mater.* **2018**, *17*, 174–179. [CrossRef] [PubMed]

84. DeStefano, M.R.; Islamoglu, T.; Garibay, S.J.; Hupp, J.T.; Farha, O.K. Room-Temperature Synthesis of UiO-66 and Thermal Modulation of Densities of Defect Sites. *Chem. Mater.* **2017**, *29*, 1357–1361. [CrossRef]